NAVAL POSTGRADUATE SCHOOL

MONTEREY, CALIFORNIA

THESIS

HIGH TERAHERTZ ABSORBING NANOSCALE METAL FILMS FOR FABRICATION OF MICROMECHANICAL BI-MATERIAL THZ SENSORS

by

Christos Bolakis

June 2010

Thesis Co-Advisors: Gamani Karunasiri
Dragoslav Grbovic

Approved for public release; distribution is unlimited

THIS PAGE INTENTIONALLY LEFT BLANK

REPORT DOCUMENTATION PAGE			*Form Approved OMB No. 0704-0188*
Public reporting burden for this collection of information is estimated to average 1 hour per response, including the time for reviewing instruction, searching existing data sources, gathering and maintaining the data needed, and completing and reviewing the collection of information. Send comments regarding this burden estimate or any other aspect of this collection of information, including suggestions for reducing this burden, to Washington headquarters Services, Directorate for Information Operations and Reports, 1215 Jefferson Davis Highway, Suite 1204, Arlington, VA 22202-4302, and to the Office of Management and Budget, Paperwork Reduction Project (0704-0188) Washington DC 20503.			
1. AGENCY USE ONLY *(Leave blank)*	**2. REPORT DATE** June 2010	**3. REPORT TYPE AND DATES COVERED** Master's Thesis	
4. TITLE AND SUBTITLE High Terahertz Absorbing Nanoscale Metal Films for Fabrication of Micromechanical Bi-material THz Sensors		**5. FUNDING NUMBERS**	
6. AUTHOR(S) Christos Bolakis			
7. PERFORMING ORGANIZATION NAME(S) AND ADDRESS(ES) Naval Postgraduate School Monterey, CA 93943-5000		**8. PERFORMING ORGANIZATION REPORT NUMBER**	
9. SPONSORING /MONITORING AGENCY NAME(S) AND ADDRESS(ES) N/A		**10. SPONSORING/MONITORING AGENCY REPORT NUMBER**	
11. SUPPLEMENTARY NOTES The views expressed in this thesis are those of the author and do not reflect the official policy or position of the Department of Defense or the U.S. Government.			
12a. DISTRIBUTION / AVAILABILITY STATEMENT Approved for public release; distribution is unlimited.		**12b. DISTRIBUTION CODE**	

13. ABSTRACT (maximum 200 words)

The terahertz (THz) region of the electromagnetic spectrum covers frequencies ranging from approximately 100 GHz to 10 THz. This region of the spectrum has not been fully utilized due to the lack of compact and efficient sources as well as detectors. The aim of the present research is to explore the use of thin metal films as high THz absorbing materials and determine their THz absorbing characteristics analytically as well as experimentally. The films are to be used in bi-material based suspended structure, which sense minute changes in temperature due to THz absorption via difference in thermal expansion coefficients. The amount of deformation can be measured by reflecting a light beam from the pixel structure to determine the THz power incident on it. During the initial phase, design and fabrication of efficient THz absorbing multi-layer stack was carried out. The stack consists of a dielectric Bragg reflector and a metal film. The Bragg reflector serves to maximize reflection in the visible spectral range (required by the readout scheme), while the metal serves to provide strong absorption of THz radiation. The absorption characteristics of the stack were simulated using COMSOL finite element modeling and theoretical analysis performed using Fresnel's equations and then compared with the corresponding experimental results. The measured absorption characteristics of the stack agree well with the analysis. In addition, the thickness of the metal film was optimized for maximizing the THz absorption of the stack.

14. SUBJECT TERMS Bi-material Pixel, Terahertz Imaging, Deformation, Multi-layer stack, Terahertz Absorption, COMSOL finite element modeling, Fresnel's Equations, Dielectric Bragg reflector, FTIR Spectroscopy, maximizing the THz absorption			**15. NUMBER OF PAGES** 71
			16. PRICE CODE
17. SECURITY CLASSIFICATION OF REPORT Unclassified	**18. SECURITY CLASSIFICATION OF THIS PAGE** Unclassified	**19. SECURITY CLASSIFICATION OF ABSTRACT** Unclassified	**20. LIMITATION OF ABSTRACT** UU

NSN 7540-01-280-5500 Standard Form 298 (Rev. 2-89)
Prescribed by ANSI Std. 239-18

THIS PAGE INTENTIONALLY LEFT BLANK

Approved for public release; distribution is unlimited

HIGH TERAHERTZ ABSORBING NANOSCALE METAL FILMS FOR FABRICATION OF MICROMECHANICAL BI-MATERIAL THZ SENSORS

Christos Bolakis
Lieutenant Junior Grade, Greek Navy

Submitted in partial fulfillment of the
requirements for the degree of

MASTER OF SCIENCE IN PHYSICS

from the

NAVAL POSTGRADUATE SCHOOL
June 2010

Author: Christos Bolakis

Approved by: Gamani Karunasiri
Thesis Advisor

Dragoslav Grbovic
Co-Advisor

Andres Larraza
Chairman, Department of Physics

THIS PAGE INTENTIONALLY LEFT BLANK

ABSTRACT

The terahertz (THz) region of the electromagnetic spectrum covers frequencies ranging from approximately 100 GHz to 10 THz. This region of the spectrum has not been fully utilized due to the lack of compact and efficient sources as well as detectors. The aim of the present research is to explore the use of thin metal films as high THz absorbing materials and determine their THz absorbing characteristics analytically as well as experimentally. The films are to be used in bi-material based suspended structure, which sense minute changes in temperature due to THz absorption via difference in thermal expansion coefficients. The amount of deformation can be measured by reflecting a light beam from the pixel structure to determine the THz power incident on it. During the initial phase, design and fabrication of efficient THz absorbing multi-layer stack was carried out. The stack consists of a dielectric Bragg reflector and a metal film. The Bragg reflector serves to maximize reflection in the visible spectral range (required by the readout scheme), while the metal serves to provide strong absorption of THz radiation. The absorption characteristics of the stack were simulated using COMSOL finite element modeling and theoretical analysis performed using Fresnel's equations and then compared with the corresponding experimental results. The measured absorption characteristics of the stack agree well with the analysis. In addition, the thickness of the metal film was optimized for maximizing the THz absorption of the stack.

THIS PAGE INTENTIONALLY LEFT BLANK

TABLE OF CONTENTS

I. INTRODUCTION....1

II. THEORY AND MODELING....5
- A. THEORETICAL BACKGROUND....5
- B. FINITE ELEMENT MODELING....12
  - 1. Drawing the Multi-layer Stack....12
  - 2. Subdomain Settings....13
  - 3. Boundary Settings....14
  - 4. Meshing the Stack and Solving....16
  - 5. Comparison of the Absorption Results....16

III. MEASUREMENT OF THZ CHARACTERISTICS....19
- A. FUNDAMENTALS OF FTIR SPECTROSCOPY....19
  - 1. The Electromagnetic Aspect of the FTIR....19
  - 2. Description of Some Basic FTIR Parameters....20
- B. DESCRIPTION OF THE MULTILAYER STACK....21
- C. MEASURMENT OF TRANSMISSION COEFFICIENT....21
- D. MEASUREMENT OF REFLECTION COEFFICIENT....24
- E. DETERMINATION OF ABSORPTION....28

IV. DISCUSSION AND ANALYSIS....31
- A. INITIAL COMPARISONS....31
- B. ANALYSIS AND OPTIMIZATION....36

V. CONCLUSION....43

APPENDIX A: MATLAB CODE DEVELOPED FOR CALCULATING THE TOTAL POWER REFLECTION OF THE MULTI-LAYER STACK....45

APPENDIX B: MATLAB CODE DEVELOPED FOR CALCULATING THE TOTAL POWER TRANSMISSION OF THE MULTI-LAYER STACK....47

LIST OF REFERENCES....51

INITIAL DISTRIBUTION LIST....53

THIS PAGE INTENTIONALLY LEFT BLANK

LIST OF FIGURES

Figure 1. The readout process begins by recording a background image using the reflected visible light from the array placed into the vacuum cell, when the THz source is off. After the THz illumination, through the lens and the wrapped object, the respective pixels which absorb that radiation will deform. As a result, all of or portion of the light reflected from the pixel array will be blocked by the aperture and result in the different amount of light reaching the CCD. By subtracting the background image, one can obtain the image (shadow) of the non THz transparent object. 2

Figure 2. Schematics of the Bi-material Pixel's Optimized for THz Frequencies 3

Figure 3. Simulated Deformation of the Pixel in Figure 2 using COMSOL Finite Element Modeling Software 4

Figure 4. Three Layer Structure used in Calculation of Transmission and Reflection Coefficients (from [9]) 5

Figure 5. A Thin Film Stack Containing Arbitrary Number of Films (from [9]) 6

Figure 6. Structure of the Multilayer Stacks used in the Analysis and Measurement 7

Figure 7. Calculated Transmission Coefficient of the Multi-layer Stack with 15 nm of Cr Layer as a Function of THz Frequency 9

Figure 8. Calculated Transmission Coefficient of the Multi-layer Stack with 30 nm of Cr Layer as a Function of THz Frequency 9

Figure 9. Calculated Reflection Coefficient of the Multi-layer Stack with 15 nm of Cr Layer as a Function of THz Frequency 10

Figure 10. Calculated Reflection Coefficient of the Multi-layer Stack with 30 nm of Cr Layer as a Function of THz Frequency 10

Figure 11. Calculated Absorption of the Multi-layer Stack with 15 nm of Cr Layer as a Function of THz Frequency 11

Figure 12. Calculated Absorption of the Multi-layer Stack with 30 nm of Cr Layer as a Function of THz Frequency 11

Figure 13. Schematics of COMSOL Finite Elements Model 13

Figure 14. Settings of the Side Boundaries of the Stack 14

Figure 15. Setting the Analytical Expression for the Plane Wave 15

Figure 16. Theoretical Versus Modeled Absorption of the Multi-layer Stack with 15 nm of Cr as a Function of THz Frequency 17

Figure 17. Theoretical Versus Modeled Absorption of the Multi-layer Stack with 30 nm of Cr as a Function of THz Frequency 17

Figure 18. Typical Diagram of Michelson's Interferometer used in FTIR Spectroscopy 19

Figure 19. Experimental Setup for Measuring the Transmission of a Wafer 22

Figure 20. a) Experimental Setup to Collect the Background; b) Experimental Setup to Collect the Sample's Transmission 23

Figure 21. Experimental Transmission of the Multi-layer Stack of 15 nm of Cr as a Function of THz Frequency 24

Figure 22. Experimental Transmission of the Multi-layer Stack of 30 nm of Cr as a Function of THz Frequency 24
Figure 23. Experimental Setup for Measuring the Reflection of a Wafer 25
Figure 24. a) Experimental Setup to Collect the Background; b) Experimental Setup to Collect the Sample's Reflection 26
Figure 25. Experimental Reflection of the Multi-layer Stack of 15 nm of Cr as a Function of THz Frequency 27
Figure 26. Experimental Reflection of the Multi-layer Stack of 30 nm of Cr as a Function of THz Frequency 27
Figure 27. Experimental Absorption of the Multi-layer Stack with 15 nm Cr layer as a Function of THz Frequency 28
Figure 28. Experimental Absorption of the Multi-layer Stack with 30 nm Cr layer as a Function of THz Frequency 29
Figure 29. Experimental Versus Simulated Transmission Coefficient of the Multi-layer Stack with 15 nm thick Cr as a Function of THz Frequency 31
Figure 30. Experimental Versus Simulated Transmission Coefficient of the Multi-layer Stack with 30 nm thick Cr as a Function of THz Frequency 32
Figure 31. Experimental Versus Simulated Reflection Coefficient of the Multi-layer Stack with 15 nm thick Cr Layer as a Function of THz Frequency 32
Figure 32. Experimental Versus Simulated Reflection Coefficient of the Multi-layer Stack with 30 nm thick Cr Layer as a Function of THz Frequency 33
Figure 33. Experimental Versus Simulated Absorption of the Multi-layer Stack with 15 nm Cr Layer as a Function of THz Frequency 33
Figure 34. Experimental Versus Simulated Absorption of the Multi-layer Stack with 30 nm Cr Layer as a Function of THz Frequency 34
Figure 35. Simulated Absorption of the Multi-layer Stack (without Substrate) with 1 nm thick Cr Layer and Conductivity of 6.428×10^5 [S/m] as a Function of THz Frequency 37
Figure 36. Simulated Absorption of the Multi-layer Stack (without Substrate) with 5 nm thick Cr Layer and Conductivity of 6.520×10^5 [S/m] as a Function of THz Frequency 37
Figure 37. Simulated Absorption of the Multi-layer Stack (without Substrate) with 8 nm thick Cr Layer and Conductivity of 6.589×10^5 [S/m] as a Function of THz Frequency 38
Figure 38. Simulated Absorption of the Multi-layer Stack (without Substrate) with 10 nm thick Cr Layer and Conductivity of 6.635×10^5 [S/m] as a Function of THz Frequency 38
Figure 39. Simulated Absorption of the Multi-layer Stack (without Substrate) with 11 nm thick Cr Layer and Conductivity of 6.658×10^5 [S/m] as a Function of THz Frequency 39
Figure 40. Simulated Absorption of the Multi-layer Stack (without Substrate) with 13 nm thick Cr Layer and Conductivity of 6.704×10^5 [S/m] as a Function of THz Frequency 39

Figure 41. Simulated Absorption of the Multi-layer Stack (without Substrate) with 23 nm thick Cr Layer and Conductivity of 6.934 x 10^5 [S/m] as a Function of THz Frequency.....40
Figure 42. Simulated Absorption of the Multi-layer Stack (without Substrate) with 30 nm thick Cr Layer and Conductivity of 7.095 x 10^5 [S/m] as a Function of THz Frequency.....40
Figure 43. Simualted Absorption of the Multi-layer Stack (without Substrate) as a Function of Chrome Layer Thickness.....42

THIS PAGE INTENTIONALLY LEFT BLANK

LIST OF TABLES

Table 1. Comparison of Average Coefficients for the Stack with 15 nm thick Cr Layer in the Spectral Region between 2.5 and 10 THz 35
Table 2. Comparison of Average Coefficients for the Stack with 15 nm thick Cr Layer in the Spectral Region between 2.5 and 10 THz 35
Table 3. Simulated Absorption for the Stack without the Substrate. The Middle Column gives the Conductivities used in the Simulation 41

THIS PAGE INTENTIONALLY LEFT BLANK

ACKNOWLEDGMENTS

I would like to thank Professor Gamani Karunasiri and Dr. Dragoslav Grbovic for their mentorship during the course of this research and throughout my graduate studies. Their support and guidance was direct, immense and inspiring. Moreover, I would like to thank Dr. Nick Lavric for providing the samples as well as George Jacksha and Sam Barone for providing the required technical support on the engineering aspects of this research. This work is supported in part by a grant from AFOSR.

THIS PAGE INTENTIONALLY LEFT BLANK

I. INTRODUCTION

Recently, a significant number of applications that use terahertz (THz) radiation have emerged through deeper study of the THz region of the electromagnetic spectrum (100 GHz to 10 THz). Its non-ionizing* nature and the property of being able to penetrate most of insulating materials (textiles, paper, etc.) while reflecting from metallic objects, makes it a good candidate for the leading role in applications involving detection of concealed objects and medical imaging. To name a few, in the area of homeland security THz imagers can be used to detect concealed metal objects or certain types of explosives due to their characteristics THz signatures. Moreover, in the field of medicine, THz imaging appears particularly suited for examining skin abnormalities such as skin cancer [1] and characterizing human tissues [2].

Real time imaging in THz spectral range has been achieved using an uncooled microbolometer infrared (IR) camera and a milliwatt-scale quantum cascade laser (QCL) [3]. The principle of radiation detection is based on temperature changes arising from absorption of THz by an absorbing layer within the pixel. In addition, if the material used to build the pixel exhibits a high temperature coefficient of resistance (TCR), a relative difference in its resistance will be governed by the following equation [4]:

$$R = R_o(1+\alpha\Delta\mathrm{T})$$

where R_o is the initial resistance, α is the temperature coefficient of resistance and $\Delta\mathrm{T}$ is the temperature difference.

As a result and by assuming that each pixel has been constructed in such a way that a current bias (V_b) can be applied via a Wheatstone bridge, one can measure the changes in voltage (ΔV_{out}) across the bridge as [4]:

$$\Delta V_{out} = \frac{\alpha V_b}{4}\Delta\mathrm{T} \quad \text{(assuming } \alpha\Delta\mathrm{T} \ll 1\text{)}$$

* THz photons do not carry enough energy to remove (i.e., ionize) an electron from an atom or molecule and, therefore, cannot inflict significant damage to human DNA, a fact that is opposed to X-ray imaging technique.

The disadvantage of this scheme that bias used for reading the resistance change generates heat (self heating) in the pixel which limits the integration time affecting the signal-to-noise ratio [5]. On the other hand, an alternative and more efficient read out technique is under development. This detection scheme, as shown in Figure 1, involves deformation of a bi-material based suspended structure to minute changes in temperature due to difference in thermal expansion coefficients of layers of material used to build the pixel [6]. The amount of deformation can be measured by reflecting light off from the pixel structure (see Figure 1) and observing the reflected light using a CCD camera to generate an image of THz power incident on individual pixels. Furthermore, the optical readout technique does not require any readout electronics. Consequently, self-heating effects get eliminated when at the same time longer integration times are now available and hence better signal to noise ratios [7].

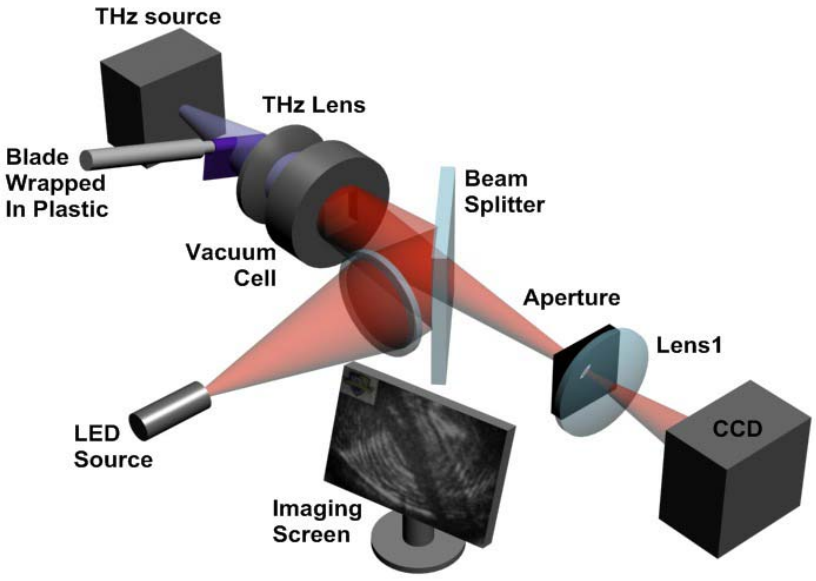

Figure 1. The readout process begins by recording a background image using the reflected visible light from the array placed into the vacuum cell, when the THz source is off. After the THz illumination, through the lens and the wrapped object, the respective pixels which absorb that radiation will deform. As a result, all of or portion of the light reflected from the pixel array will be blocked by the aperture and result in the different amount of light reaching the CCD. By subtracting the background image, one can obtain the image (shadow) of the non THz transparent object.

The pixel architecture, as displayed in Figure 2, undergoes a deformation due to absorption of certain amount of radiation. This deformation is achieved by designing the detector pixel to have areas of bi-material layers. The bi-material layers usually consist of an insulator and a metal with different coefficients of thermal expansion. When the temperature increases, these layers expand at different rates causing the whole structure to deform as shown in Figure 3. It has been shown that the use of SiO_2-Al combination can provide a significant large deflection when operates in IR wavelengths [7]. Having high sensitivity in mind, it is expected that this type of detector would be appropriate for detection of THz radiation. Note that the power density in THz spectral band in the thermal background is much smaller than that of the infrared. For achieving high sensitivity in THz frequencies, it is important to develop strong THz absorbing membrane to integrate onto the pixel.

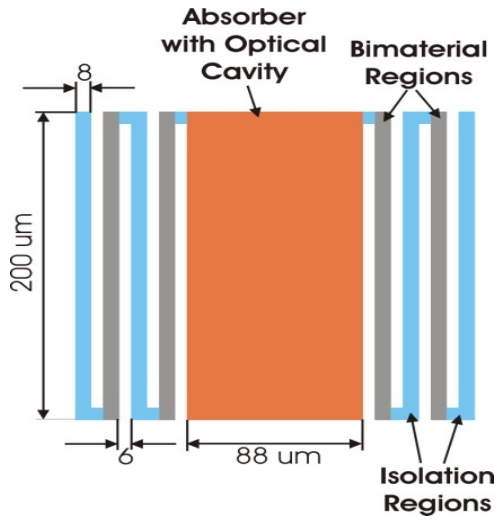

Figure 2. Schematics of the Bi-material Pixel's Optimized for THz Frequencies

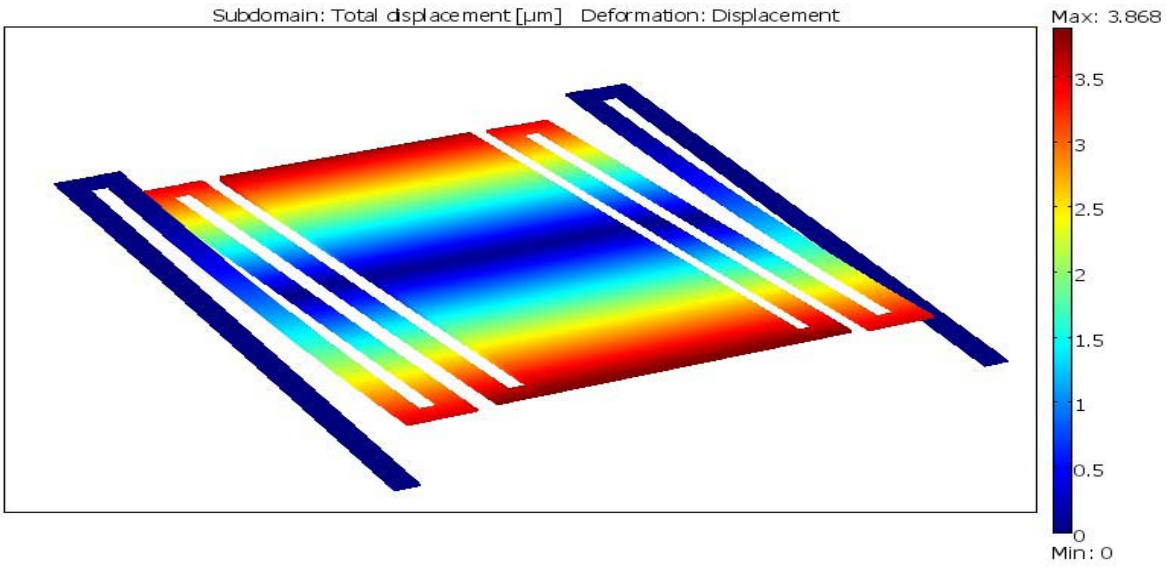

Figure 3. Simulated Deformation of the Pixel in Figure 2 using COMSOL Finite Element Modeling Software

In this thesis, THz absorption characteristics of the membrane (i.e., a multi-layer stack of thin films) will be simulated using COMSOL finite element modeling and by theoretical analysis done using Fresnel's equations. The aim is to develop a model that can estimate the absorption properties of multilayer stacks in the THz region that can be used to design sub-wavelength thin films with the maximum percentage of absorption of THz radiation. The experimental absorption measurements carried out using Fourier transform infrared spectroscopy (FTIR) of a thin-film stack developed in collaboration with Oakridge National Laboratory will also be presented [8].

II. THEORY AND MODELING

A. THEORETICAL BACKGROUND

Absorption of electromagnetic radiation in a thin film stack containing both dielectric and metal films can be calculated by determining transmission and reflection coefficients as described in [9]. The percentage of absorption is then estimated by subtracting the two coefficients from the unity. In the following, the procedure described in [9] to calculate transmission and reflection coefficients is outlined by initially assuming a simple, three-layer stack as illustrated in Figure 4.

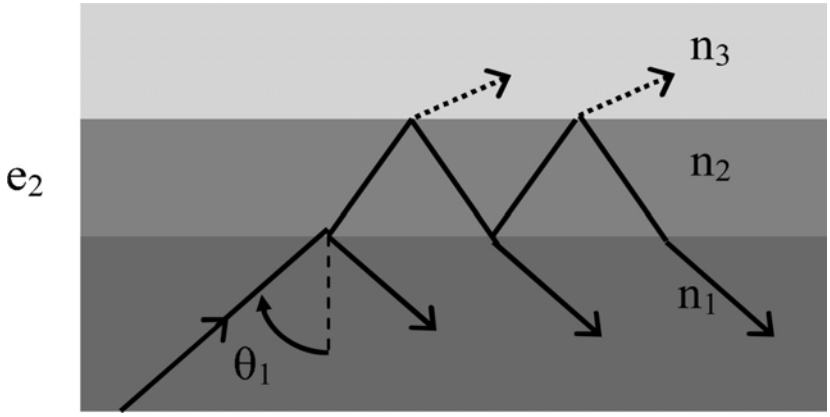

Figure 4. Three Layer Structure used in Calculation of Transmission and Reflection Coefficients (from [9])

The bottom and the top layer are simply air while the middle layer can be any material. The total reflection and transmission coefficients including multiple reflections in the film can be expressed as [9 and 10]:

$$r_2 = \frac{r_{1,2} + r_{2,3}\,\mathrm{e}^{-2j\varphi_2}}{1 + r_{1,2}r_{2,3}\,\mathrm{e}^{-2j\varphi_2}} \tag{1}$$

and

$$t_2 = \frac{t_{1,2}t_{2,3}\,\mathrm{e}^{-j\varphi_2}}{1 + r_{1,2}r_{2,3}\,\mathrm{e}^{-2j\varphi_2}}, \tag{2}$$

where $r_{k,m}$ and $t_{k,m}$ are the Fresnel coefficients of reflection and transmission, respectively, between layers k and m, and φ_κ is the phase change when propagating through layer k. Such a phase change is given by

$$\varphi_\kappa = \frac{2\pi}{\lambda} n_k d_k \cos\theta_k , \tag{3}$$

where λ is the free space wavelength, n_k is the index of refraction of layer k, d_k is its thickness, and θ_k is the associated term of the Snell's law. The index of refraction of a metal thin film can be described by Equation 4 [10]. The complex nature of the index of refraction reflects the absorptive nature of the metal layer. The absorption of the incoming radiation will depend on the conductivity (σ) of the metal.

$$n_k = (1-i)\sqrt{\sigma/(4\pi\varepsilon_0 f)} , \tag{4}$$

where f is the frequency of incident radiation.

This approach can be generalized for a stack containing arbitrary number of films, as depicted in Figure 5.

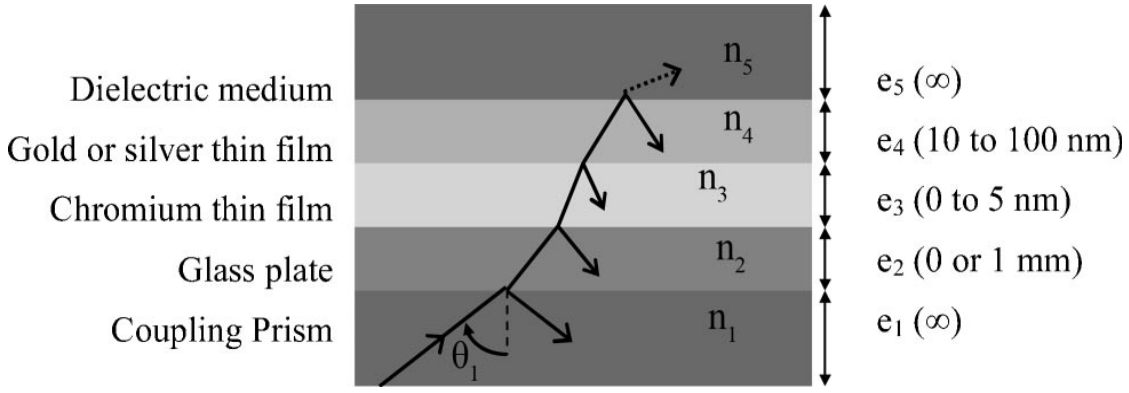

Figure 5. A Thin Film Stack Containing Arbitrary Number of Films (from [9])

The reflection and transmission coefficients can be obtained using the following recursive formulas [9 and 10]:

$$r_i = \frac{r_{i-1,i} + r_{i+1} e^{-2j\varphi_i}}{1 + r_{i-1,i} r_{i+1} e^{-2j\varphi_i}} \tag{5}$$

and

$$t_i = \frac{t_{i-1,i} t_{i+1} e^{-j\varphi_i}}{1 + r_{i-1,i} r_{i+1} e^{-2j\varphi_i}}, \tag{6}$$

where r_i and t_i are the total coefficients of reflection and transmission respectively from i-th layer and above. Note that by assuming that the very first and last layers to be air, the counter i starts from the second layer from the top and goes until 2 (i.e., in Figure 5 where there are 5 layers, i starts from 4). A computer program was developed (see appendices A and B) to calculate the total reflection (fraction of the incoming power reflected) $r_2 r_2^*$ and transmission (fraction of the incoming power transmitted) $\frac{\cos\theta_{out}}{\cos\theta_{in}} t_2 t_2^*$ coefficients as a function of THz frequency, where θ_{in} and θ_{out} are the angles of incidence and transmission, respectively. By subtracting the reflection and transmission coefficients from the unity, absorption in the stack can be obtained as

$$A = 1 - r_2 r_2^* - \frac{\cos\theta_{out}}{\cos\theta_{in}} t_2 t_2^* \quad . \tag{7}$$

The multi-layer stacks used in our experimental measurements consisted of the total of eleven thin films deposited on a 500 μm thick silicon substrate, as shown in Figure 6.

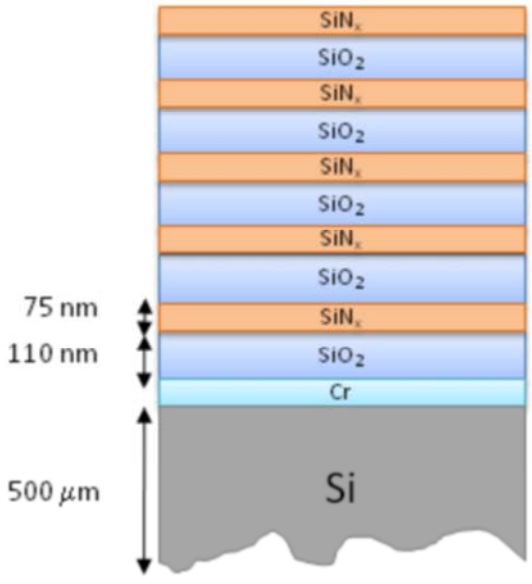

Figure 6. Structure of the Multilayer Stacks used in the Analysis and Measurement

Two multilayer stacks consists of thin Cr film of thickness either 15 nm or 30 nm was first grown on Si substrate followed by five successive periods of SiO_2 and Si_3N_4 with thicknesses of 110 nm and 75 nm, respectively. The SiO_2 and Si_3N_4 layers act as a Bragg reflector for optical readout of pixel deflection as well as impedance matching to reduce the reflection at the metal interface. The indices of refraction we used for the dielectric materials SiO_2 and Si_3N_4 were 1.46 and 2.05 respectively. From equation (4), which gives the corresponding complex index of refraction for Cr, the direct dependence of the conductivity of the metal of interest is apparent. The conductivities of Cr layers have been measured using a 4-point probing method and found to be 6.75 x 10^5 [S/m] and 7.2 x 10^5 [S/m] for 15 nm and 30 nm layers, respectively. These values are consistent with the measurements by Laman et al. [11] which showed that the conductivity of thin films is much lower than that of a bulk material due to high surface scattering. The complex index of refraction for the Si substrate was calculated using the following equation [12].

$$n_{si} = \sqrt{\varepsilon_r} - i\frac{\sigma\lambda}{0.033\sqrt{\varepsilon_r}} \tag{8}$$

Where ε_r is the relative dielectric constant of silicon and σ is the conductivity of the silicon substrate. For the substrate used for the structure, the conductivity is about 10 [S/m].

Using equations (1)–(8), the transmission, reflection and absorption of the two stacks consists of Cr layers of 15 nm and 30 nm were calculated for frequencies from 2.5 to 10 THz μm at an angle of incidence of 30 degrees. The results are displayed in Figures 7–12. The oscillatory behavior of the coefficients is due to the Fabry-Perot effect associated with the 500 μm thick Si substrate.

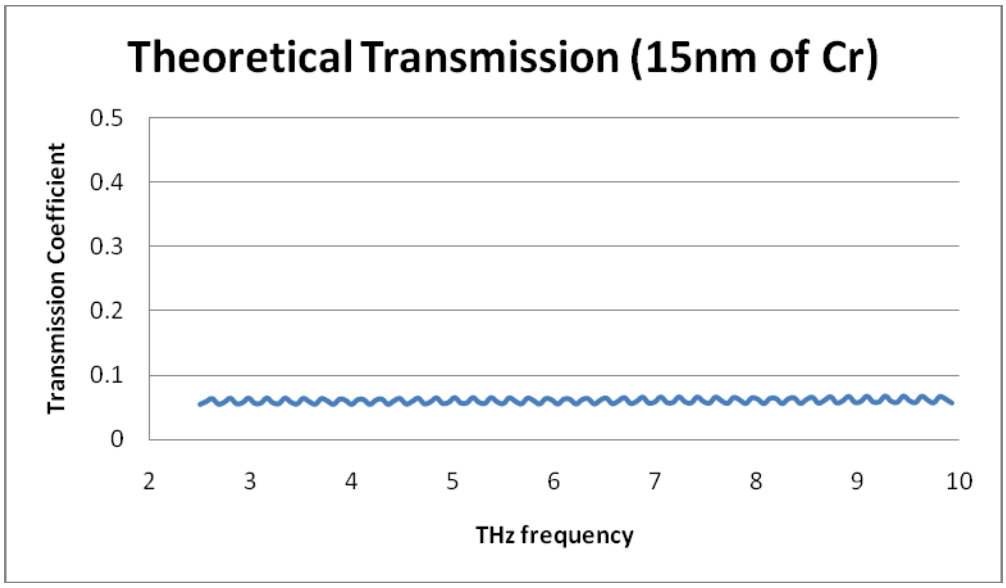

Figure 7. Calculated Transmission Coefficient of the Multi-layer Stack with 15 nm of Cr Layer as a Function of THz Frequency

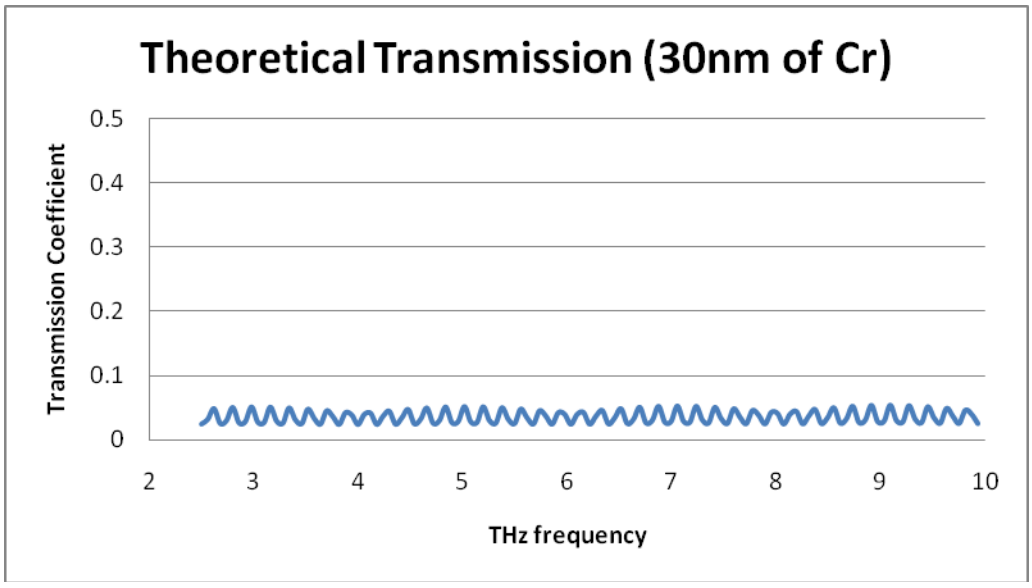

Figure 8. Calculated Transmission Coefficient of the Multi-layer Stack with 30 nm of Cr Layer as a Function of THz Frequency

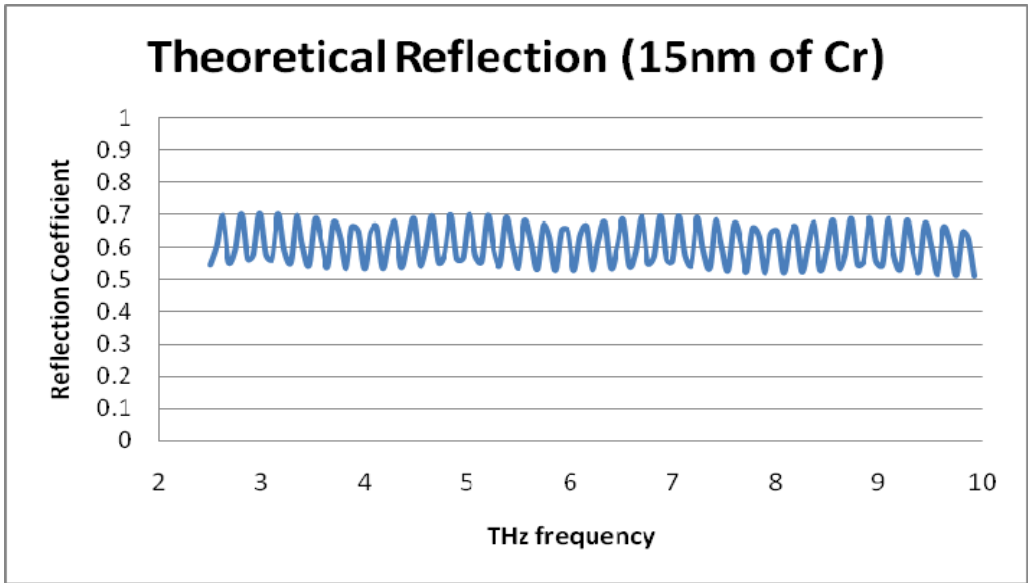

Figure 9. Calculated Reflection Coefficient of the Multi-layer Stack with 15 nm of Cr Layer as a Function of THz Frequency

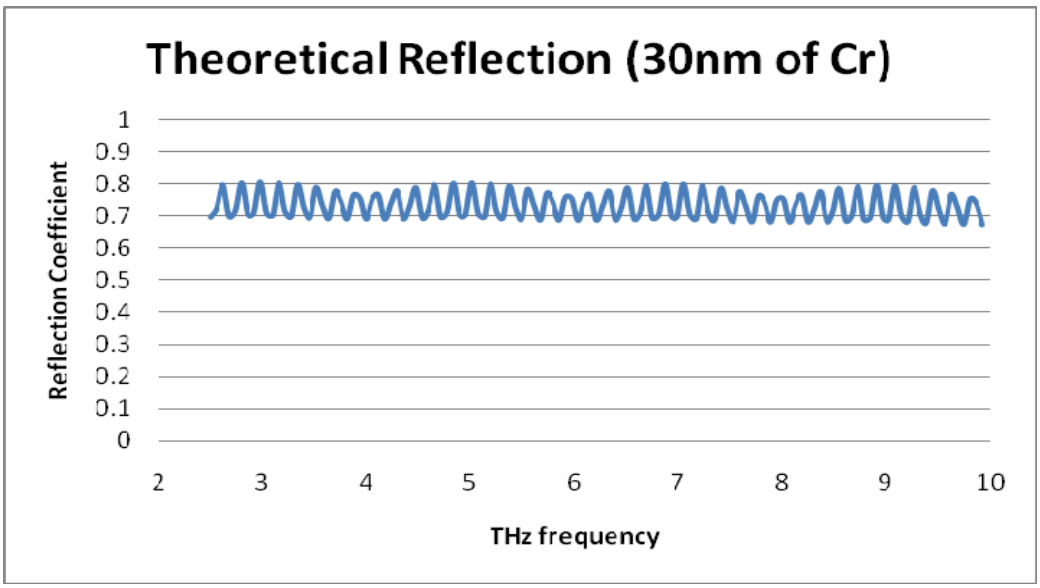

Figure 10. Calculated Reflection Coefficient of the Multi-layer Stack with 30 nm of Cr Layer as a Function of THz Frequency

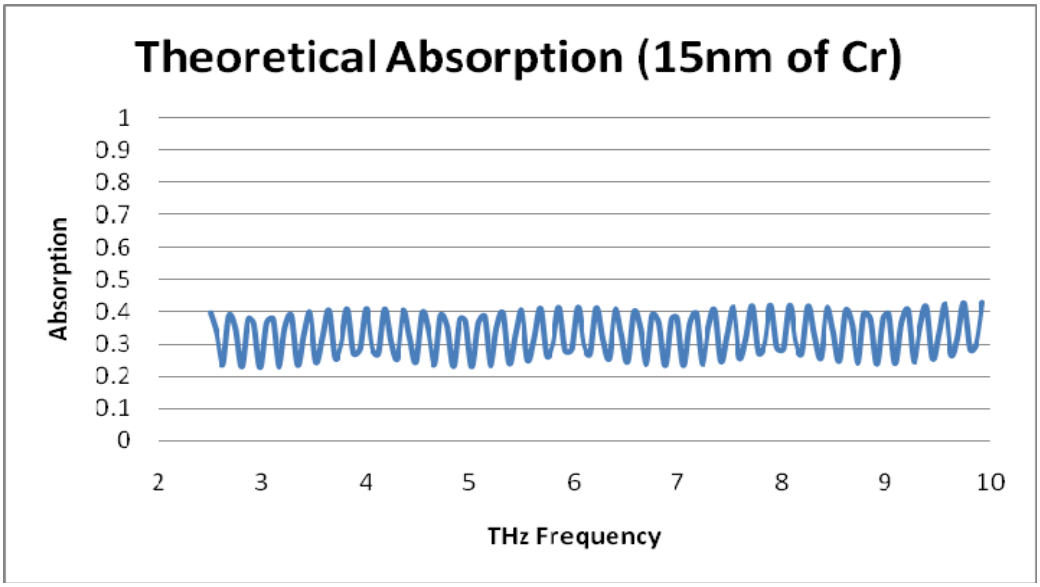

Figure 11. Calculated Absorption of the Multi-layer Stack with 15 nm of Cr Layer as a Function of THz Frequency

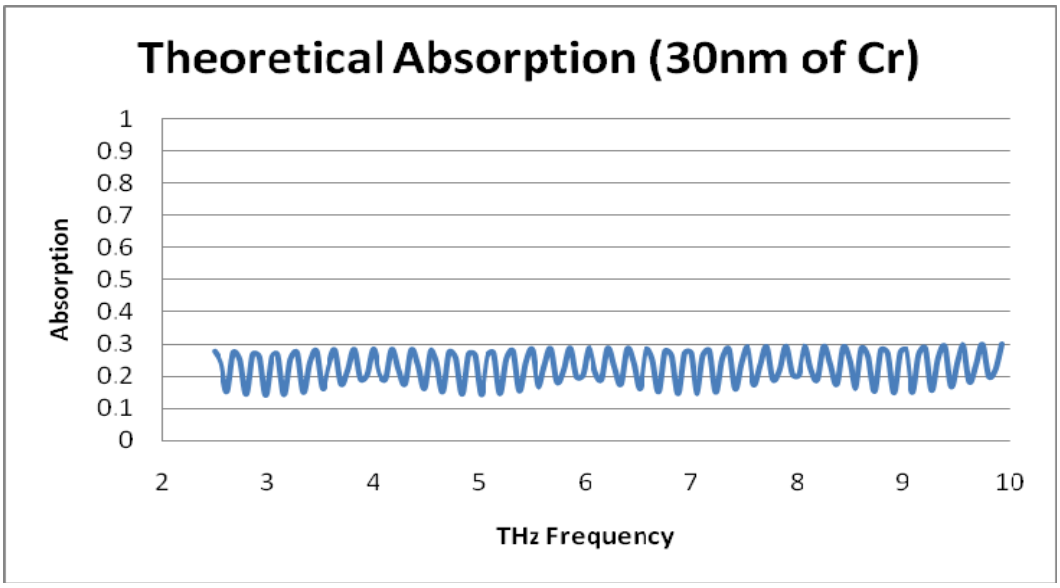

Figure 12. Calculated Absorption of the Multi-layer Stack with 30 nm of Cr Layer as a Function of THz Frequency

It can be seen from the Figures 11 and 12 that the calculated absorption is about 30% for the stack with 15 nm Cr and 20% for the one with 30 nm Cr. This is primarily

due to the high resistivity of the thinner film which generates more Joule heating and hence higher absorption. Note that above calculations give total absorption in Cr layer and Si substrate.

B. FINITE ELEMENT MODELING

The absorption characteristics of the stacks were also simulated using COMSOL finite element modeling. The main advantage of COMSOL is that it provides a convenient way to determine absorption in individual layers in the stack which is important when several layers absorb the incident radiation. However, the analytical approach developed above provides a way to compare the validity of the simulation. Before modeling using COMSOL, it is important to set appropriate physics and boundary conditions in addition to the physical dimensions of the layer structure in the stack. A detailed guidance for these necessary steps is given below [12].

1. Drawing the Multi-layer Stack

Before starting to draw the stack, an appropriate selection of the physics through the model navigator in COMSOL has to be done. The In-plane waves/Hybrid-Mode Waves/Harmonic propagation in the RF module were used in the modeling. This specific physics offers the harmonic electromagnetic waves analysis. Then the stack has to be drawn using the thicknesses exactly as they are described in the section on theoretical background. The lateral dimensions do not play any role because they are regarded as infinite by using the periodic boundary conditions. In addition, three extra layers of air have to be added on top and two at bottom by extending the very top and bottom layers so as to be at least 1 μm thick as illustrated in Figure 13. These two layers act as absorbers for the radiation exists (i.e., transmitted and reflected) from the stack.

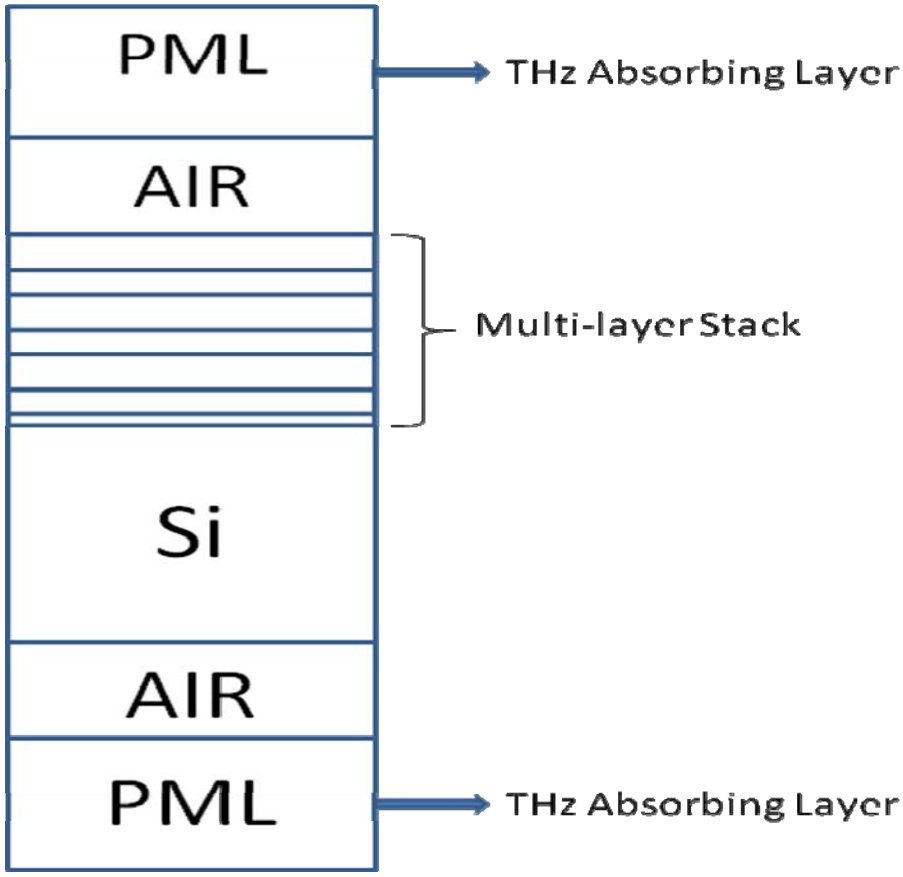

Figure 13. Schematics of COMSOL Finite Elements Model

Moreover, two composite objects were created by combining (a) the two top layers and (b) the rest of the layers. Then a boundary pair at the shared boundary of the two composite objects was created. The reason for these actions will be obvious later.

2. Subdomain Settings

After the stack has been designed, including the additional layers, the assignment of the corresponding materials for each layer has to be done. For the dielectric films, we just set $n = 1.46$ for SiO_2 and $n = 2.05$ for Si_3N_4. The refractive indices of chrome and silicon substrate are given by equations (4) and (8), respectively. These can be incorporated using the global expressions in COMSOL. Moreover, the very bottom and top extended layers (1μm) should be set to PML's with absorption along y direction.

3. Boundary Settings

The boundaries are divided into three groups. The first group includes the very top, the very bottom and the boundary pair (between the two composite objects). These boundaries should be set as perfect magnetic conductors. For the second group, which includes the other inner boundaries, the default setting (continuity) should be left unchanged. The settings for the third group corresponding to boundaries along the two sides are shown in Figure 14.

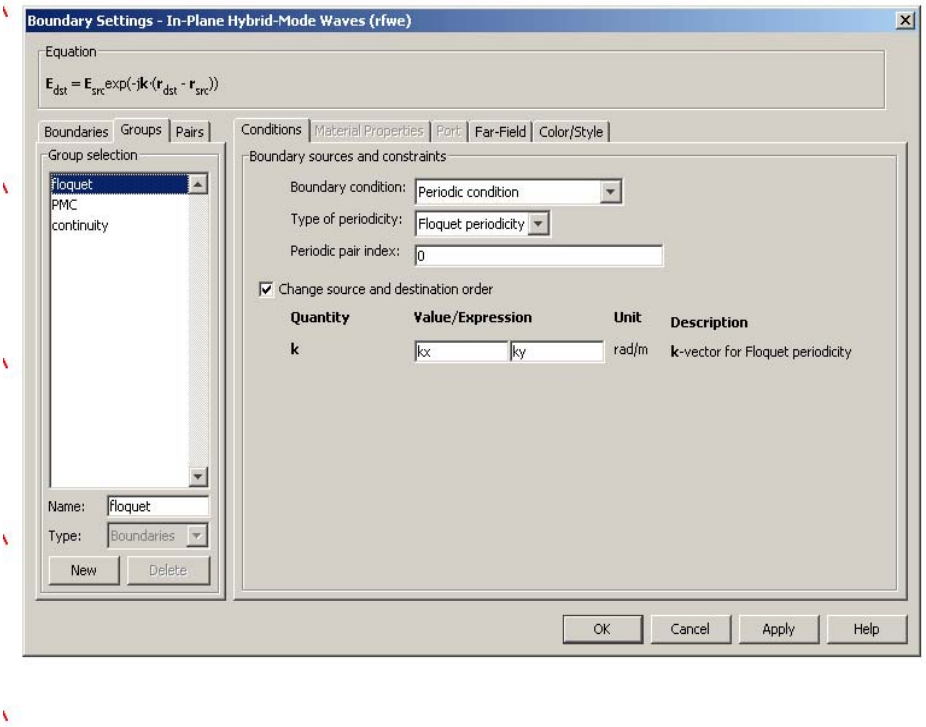

Figure 14. Settings of the Side Boundaries of the Stack

Above, k_x and k_y are the x and y components of the k-vector respectively and they can also defined k_y in global expressions as

$$k_x = k\sin(\theta), \tag{9}$$

$$k_y = k\cos(\theta), \tag{10}$$

$$k = \frac{2\pi}{lambda0\_rfweh} \ , \tag{11}$$

where θ is the angle of incidence of the plain electromagnetic wave on the stack.

Now focusing on the boundary pair at the boundaries between the two composite objects that has been created, this pair has to be set to the port boundary condition and the input power to be 1 Watt. Moreover, an analytical expression for the plane wave is required as shown in Figure 15.

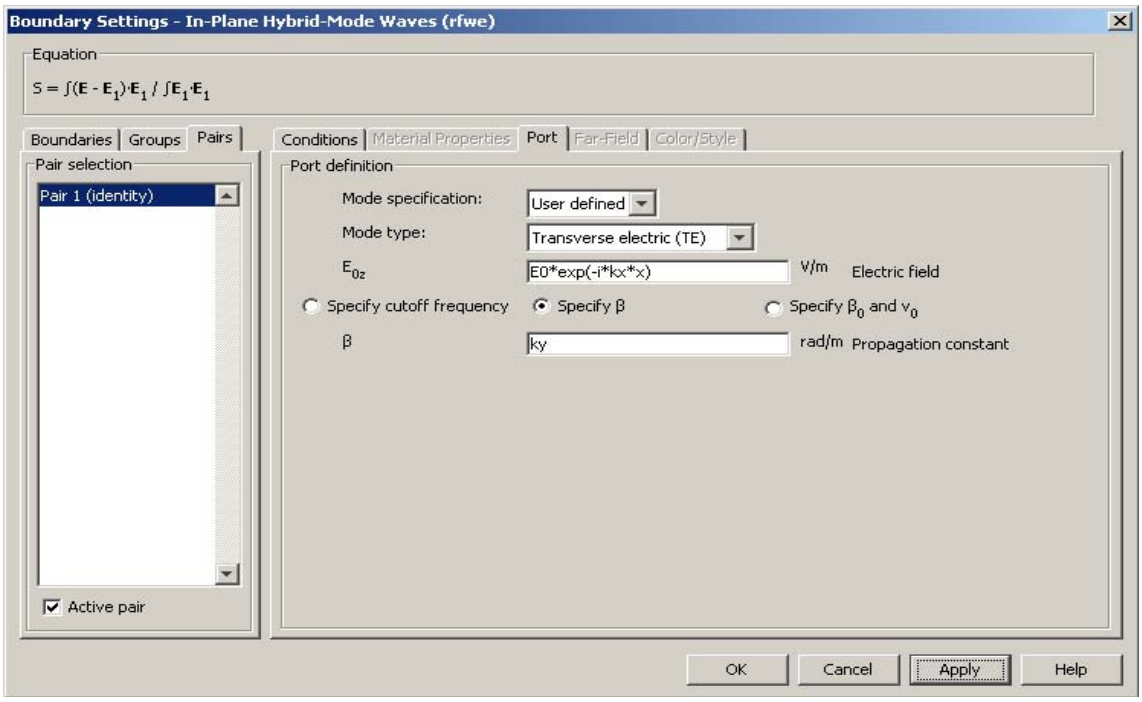

Figure 15. Setting the Analytical Expression for the Plane Wave

After having done that, an incident field can be applied at the source boundary, and will only propagate in one direction into the domain, where it may reflect back. In addition, any reflected wave will pass back through the pair boundary unimpeded. Note that the source boundary is colored cyan and the destination purple by default. The source has to be at the bottom of the destination.

4. Meshing the Stack and Solving

In order to follow the Nyquist theorem [14], at least eight mesh elements need to be present for each wavelength length. Since we work with very long wavelengths compared to the film thicknesses, i.e., from 30 μm to 120 μm, that rule does not play a significant role to our modeling procedure. Moreover, even our model is not symmetric (since we include the 500 μm Si substrate) and a manual meshing through sweeping methods should be necessary, a simple automatic mesh refining will work.

By solving the problem for an angle of incidence of 30 degrees and wavelengths from 30 μm to 120 μm, we then can reproduce the corresponding reflection and transmission power (nPoav_rfweh) by simply using the postprocessing function in COMSOL and integrating it over the inner boundaries of the top and bottom PMLs, respectively.

5. Comparison of the Absorption Results

After subtracting the reflected and transmitted powers of the stack from 1 W of incident power, the amount of absorbed power by the stack can be estimated. The square points in Figures 16 and 17 show the modeled absorption for 15 and 30 nm stacks, respectively as a function of THz frequency. The solid lines in Figures 16 and 17 show the calculated absorption indicating a good agreement between the two approaches.

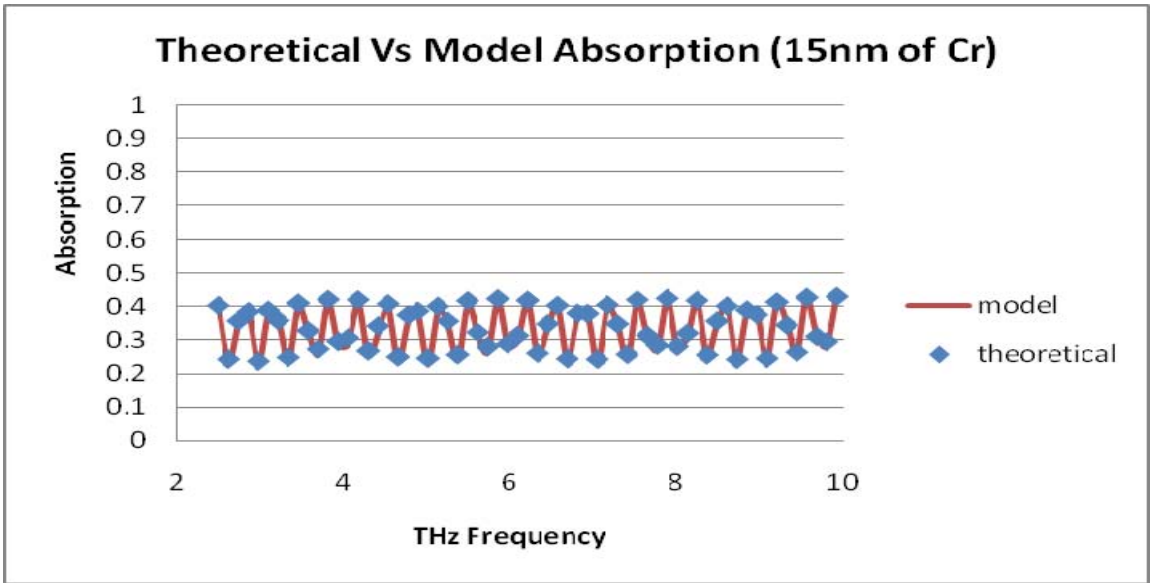

Figure 16. Theoretical Versus Modeled Absorption of the Multi-layer Stack with 15 nm of Cr as a Function of THz Frequency

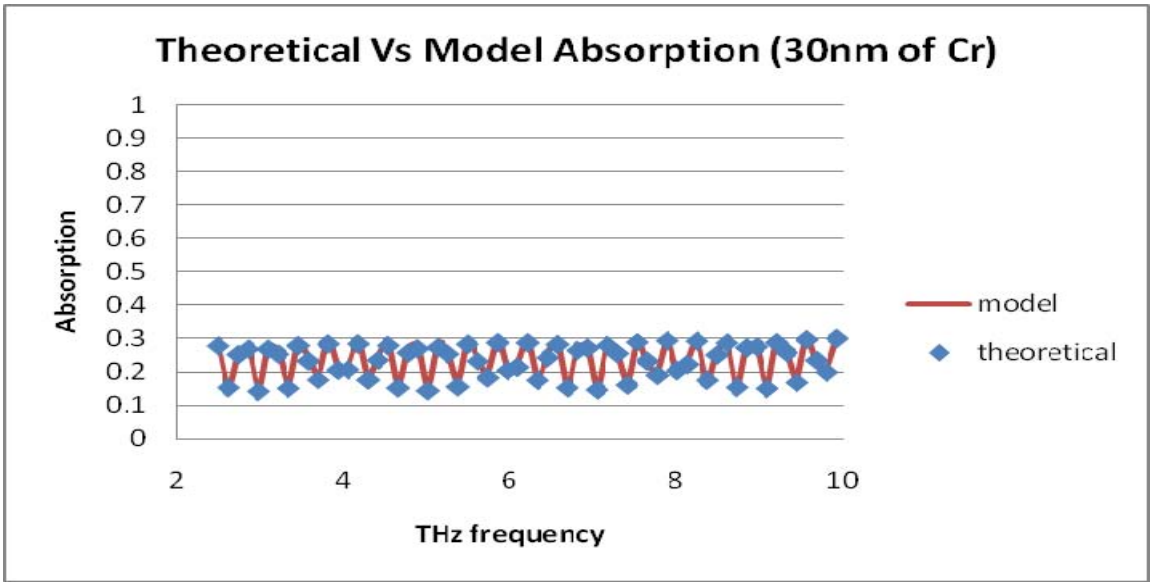

Figure 17. Theoretical Versus Modeled Absorption of the Multi-layer Stack with 30 nm of Cr as a Function of THz Frequency

THIS PAGE INTENTIONALLY LEFT BLANK

III. MEASUREMENT OF THZ CHARACTERISTICS

A. FUNDAMENTALS OF FTIR SPECTROSCOPY

The main instrument for conducting all the experimental measurements required for the absorption of thin-film materials in the THz range, was the NEXUS 870 FTIR. The incident THz radiation on the sample undergoes (a) reflection, (b) absorption and (c) transmission. The instrument is capable of measuring the intensity of radiation passing through the sample or reflecting from it. The transmission and reflection coefficients can be determined by measuring the same quantities either without the same or using a perfect reflector (gold coated mirror), respectively for subtracting the background. This process allows for a quantitative analysis of the resulting absorption of any multi-layer stack of interest.

1. The Electromagnetic Aspect of the FTIR

The functionality of the FTIR is based on a Michelson interferometer as shown in Figure 18. The light from a globar source in the FTIR spectrometer is divided at the beamsplitter, then reflected at either the translating or fixed mirror, and finally recombined at the beamsplitter to proceed to the sample area and the detector [7].

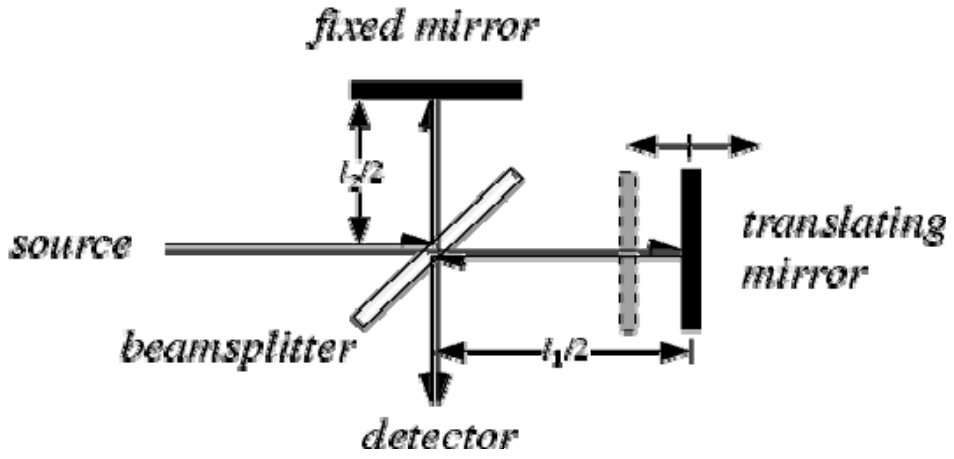

Figure 18. Typical Diagram of Michelson's Interferometer used in FTIR Spectroscopy

If the incoming electromagnetic wave is represented by:

$$\vec{E} = \overrightarrow{E_m}\cos(\omega t - 2\pi\kappa y), \tag{12}$$

where E_m is the average electric field amplitude and κ the corresponding modified wavenumber ($\kappa = \frac{1}{\lambda}$ [cm^{-1}]), the detected intensity, I(x), as a function of the translating mirror's displacement, x, is given by [8]

$$\mathrm{I}(x) = \mathrm{I}(\kappa)[1 + \cos(2\pi\kappa x)]. \tag{13}$$

In addition, one of the advantages of the FTIR is that many different wavenumbers due to a broadband source can be analyzed simultaneously. Thus, by first integrating over the wavenumbers and then taking Fourier transform of it, one can obtain a formula for the detected intensity as a function of the modified wavenumber κ as,

$$\mathrm{I}(k) = \int_0^\infty [I(x) - \frac{I(0)}{2}]\cos(2\pi kx)dx \ . \tag{14}$$

The software package (Omnic) came with the NEXUS 870 FTIR spectrometer perform the analysis based on the formula in equation (14) for extracting the spectral information.

2. Description of Some Basic FTIR Parameters

Before conducting any experimental measurement, the adjustment of some basic parameters of FTIR is recommended [15]. To name a few, the gain, the resolution, the number of scans and the velocity of the moving mirror. The default setting for the gain is the autogain. The adjustment of parameters to enhance specific signals has to be done with caution to avoid the saturation of the detector. There may be cases when a manual adjustment of the gain is necessary. The resolution has to do with the how sharp peaks in the spectrum can be resolved. The sharper the peaks in the spectrum the higher resolution needed. The default setting for the resolution in wavenumbers is 4 [cm^{-1}], which correspond to an average data spacing of 2 [cm^{-1}]. The number of scans in combination

with the velocity of the moving mirror can play a significant role for the improvement of the signal-to-noise ratio. The default settings for the number of scans and mirror's velocity are 32 and 6.3 [$\frac{cm}{s}$], respectively.

B. DESCRIPTION OF THE MULTILAYER STACK

The multi-layer stacks used in our experimental measurements consisted of eleven thin films in total deposited on a 500μm thick silicon substrate, as shown in Figure 6. The detailed description of the two multilayer stacks used was given in Chapter II.

The experimental measurements of the transmission and reflection coefficients of the stacks were conducted by using the Fourier transform interferometer (FTIR). By subtracting the sum of coefficients of reflection and transmission from 1 for each wavelength, one can determine the experimental value for absorption. All measurements were carried out for frequencies from 2.5 -10 THz.

C. MEASURMENT OF TRANSMISSION COEFFICIENT

The experimental setup for measuring the transmission of a wafer is shown in Figure 19. Before placing the stack in the sample compartment of the FTIR, the background spectrum is collected. In other words, the light beam produced by the FTIR to simply pass through the air from the right to the left without the sample in place. After having collected the background, the sample was placed and repeated the measurement.

Figure 19. Experimental Setup for Measuring the Transmission of a Wafer

The steps of the experimental procedure are shown schematically in Figure 20 (a) and (b). By then properly adjusting the rotational base, the incident angle of light on the sample was set at 30 degrees (for reasons that will be discussed under the reflection measurement). In addition, since a relatively low transmission through the stacks was obtained by modeling (see Figures 10 and 11), it would be appropriate to reduce the speed of the moving mirror of the FTIR from the default value to increase the light throughput for attaining higher signal-to-noise ratios [15]. The rest of the parameters left unchanged to avoid saturation during the background measurement.

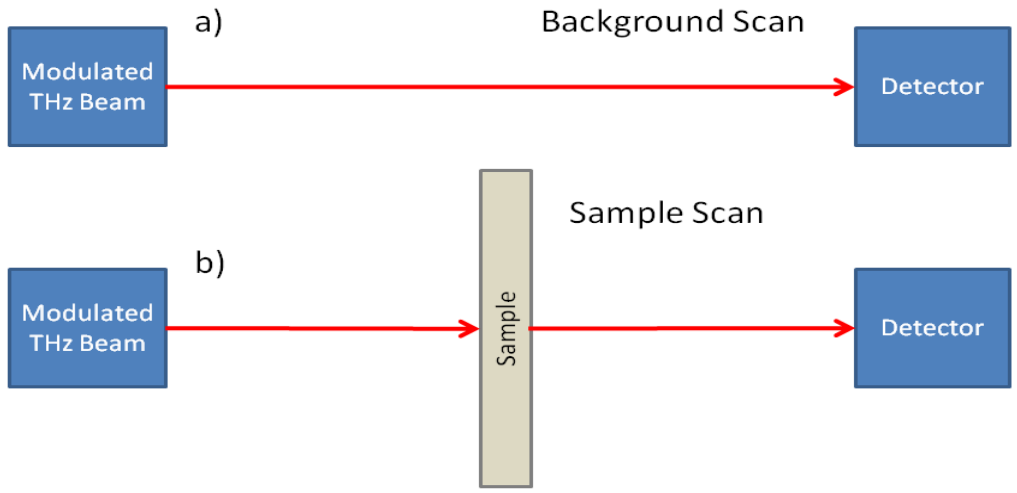

Figure 20. a) Experimental Setup to Collect the Background; b) Experimental Setup to Collect the Sample's Transmission

The measured transmission coefficients for the two stacks with 15 nm and 30 nm of Chrome layers as a function of THz frequency in 2.5 to 10 THz range are shown in Figures 21 and 22, respectively. The measured spectra are in close agreement with that of the theoretical shown Figures 7 and 8, respectively. In order to determine the absorption in the stacks, it is necessary to measure the reflection coefficients which will be described next.

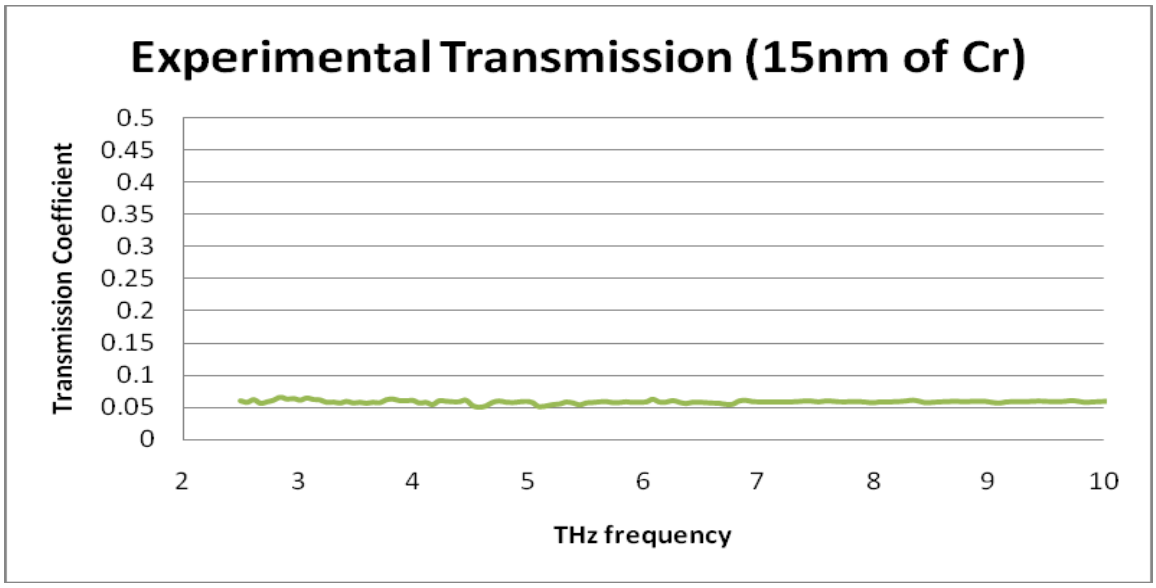

Figure 21. Experimental Transmission of the Multi-layer Stack of 15 nm of Cr as a Function of THz Frequency

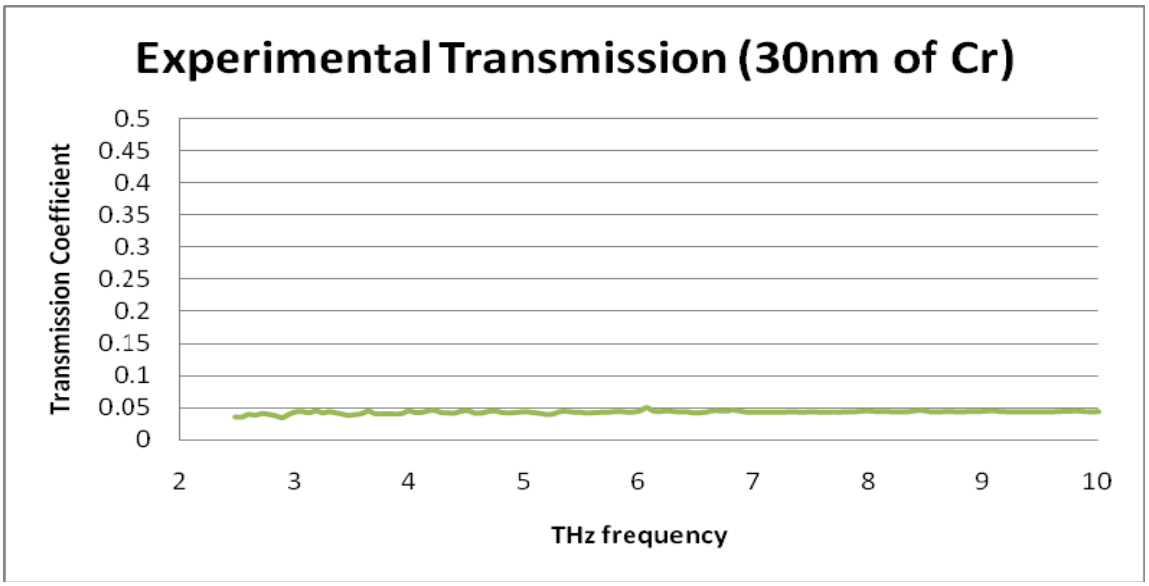

Figure 22. Experimental Transmission of the Multi-layer Stack of 30 nm of Cr as a Function of THz Frequency

D. MEASUREMENT OF REFLECTION COEFFICIENT

The experimental setup used for measuring the reflection of a wafer is depicted in Figure 23. The light beam from the FTIR was steered by placing two gold coated mirrors on the base at a fixed angle of 60 degrees with respect to their axis of symmetry. This

corresponds to a 30 degrees angle of incidence on the sample. The background measurement was dome using a gold coated silicon wafer which behaves as a perfect mirror with close to 100% reflection. At this point, it is obvious why the angle of incidence for the transmission measurement was 30 degrees.

Figure 23. Experimental Setup for Measuring the Reflection of a Wafer

Again, the successive steps of the experimental procedure are schematically illustrated in Figures 24 (a) and (b). Since the simulated reflection from the stacks (see Figures 9 and 10) was relatively high the default settings of the FTIR were used in the measurement. The background measurement was carried out using a gold coated Si wafer to subtract the background from the sample, as shown in Figure 24 (a).

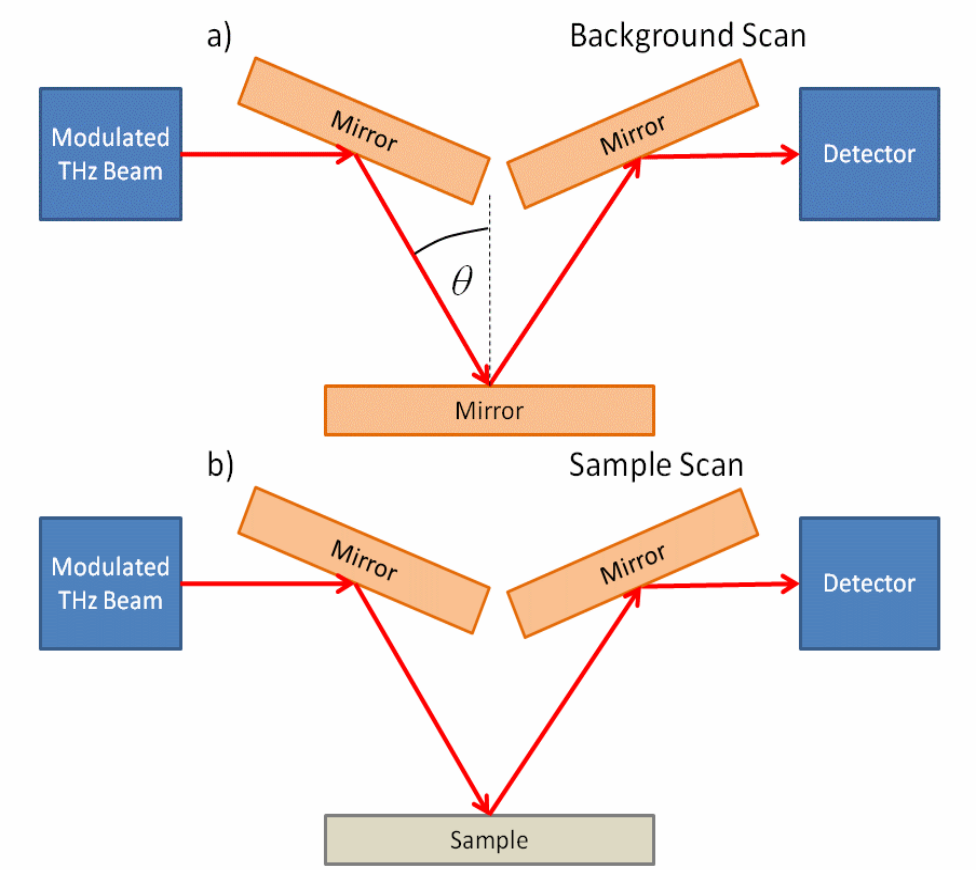

Figure 24. a) Experimental Setup to Collect the Background; b) Experimental Setup to Collect the Sample's Reflection

The measured reflection coefficients of the stacks with 15 nm and 30 nm of Chrome as a function of THz frequency are shown in Figures 25 and 26. The measured spectra are again in good agreement with that of the theoretical as shown in Figures 9 and 10.

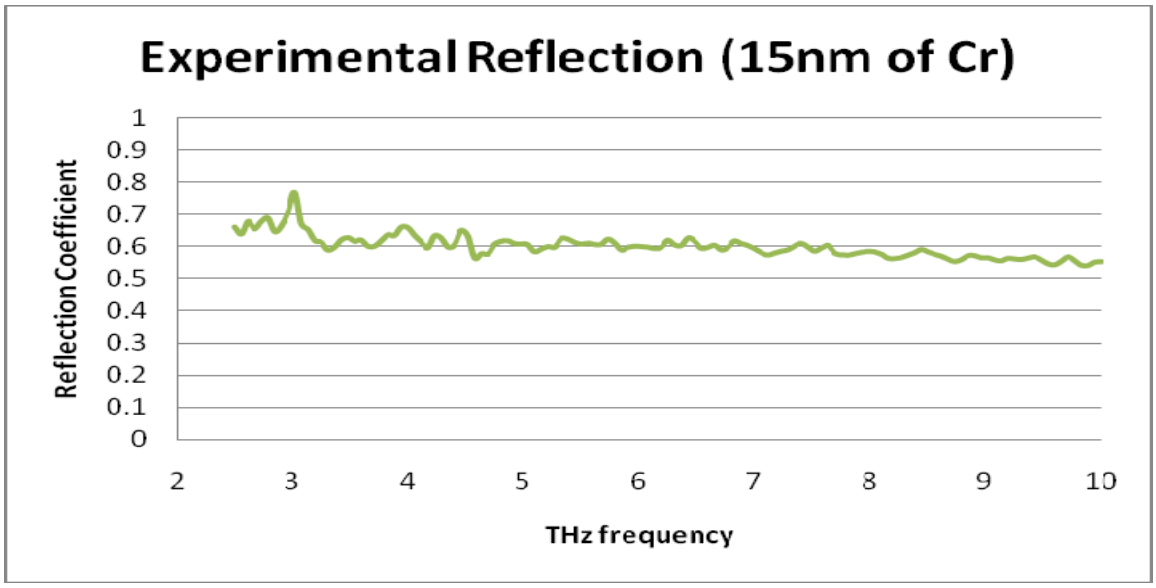

Figure 25. Experimental Reflection of the Multi-layer Stack of 15 nm of Cr as a Function of THz Frequency

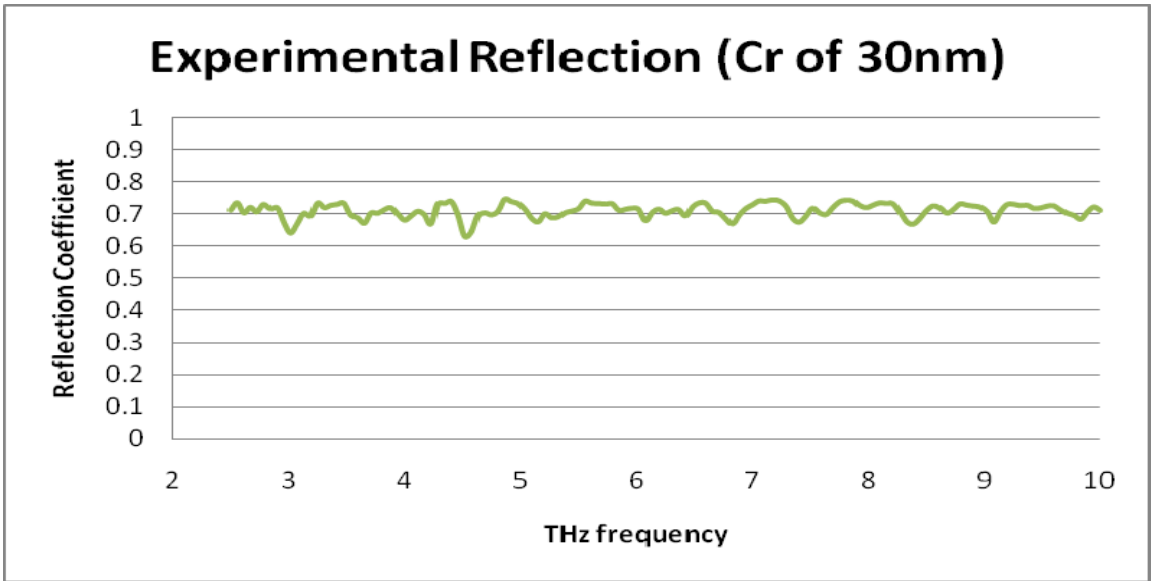

Figure 26. Experimental Reflection of the Multi-layer Stack of 30 nm of Cr as a Function of THz Frequency

E. DETERMINATION OF ABSORPTION

In order to determine the experimental absorption of the stacks, one can subtract the sum of reflection and transmission coefficients from 1 for each frequency. The respective experimental results for the absorption of the stacks of 15 nm and 30 nm of Chrome as a function of the corresponding THz frequency are shown in Figures 27 and 28. Note that these spectra include the contribution from the substrate due to its conductivity. Thought the conductivity of the substrate is relatively small compared to that of the Cr layer, it thickness is very large. For applications involving microcantilevers, the film stack is used without the substrate and it is important to determine the amount of THz absorption in the stack. However, it is possible to determine the contribution from each layer by using COMSOL since allows the estimation of power dissipation in different layers in the stack [16]. In the following chapter, a comparison between the measured and simulated data and how to optimize absorption will be presented.

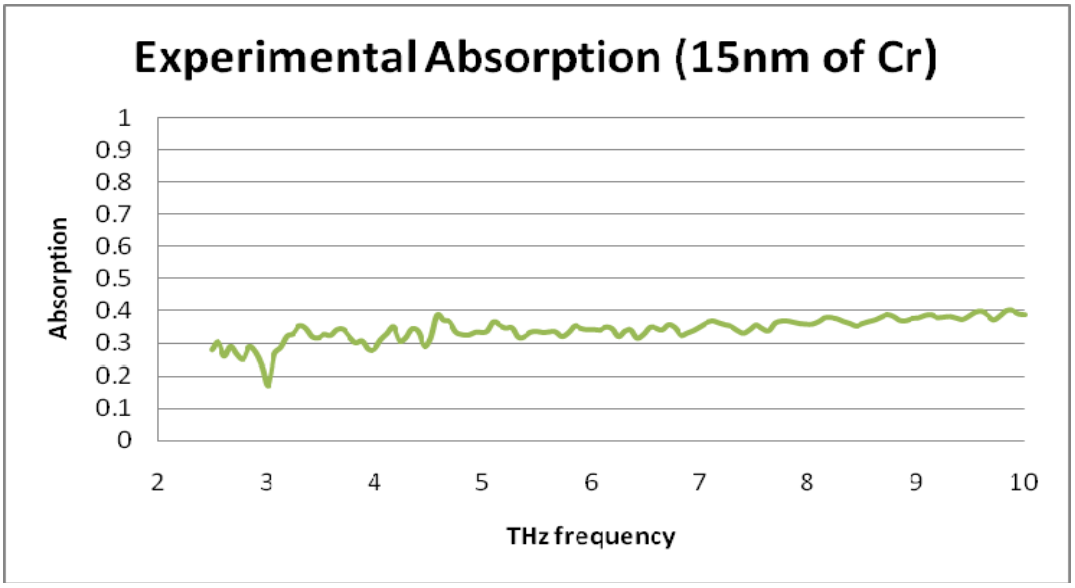

Figure 27. Experimental Absorption of the Multi-layer Stack with 15 nm Cr layer as a Function of THz Frequency

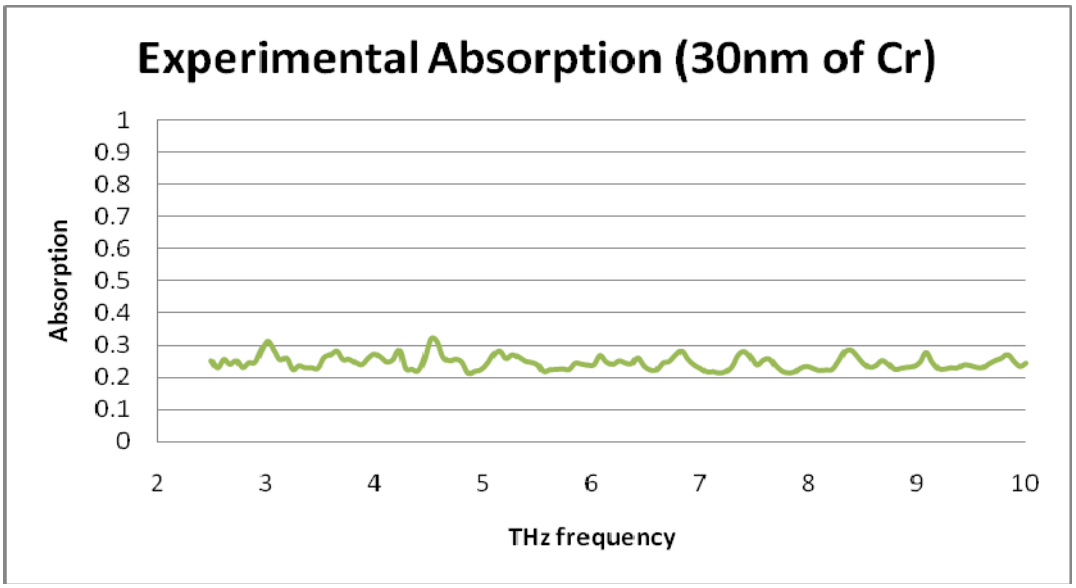

Figure 28. Experimental Absorption of the Multi-layer Stack with 30 nm Cr layer as a Function of THz Frequency

THIS PAGE INTENTIONALLY LEFT BLANK

IV. DISCUSSION AND ANALYSIS

A. INITIAL COMPARISONS

Until now we have obtained theoretical, simulation and experimental data for conducting a comparison to examine the accuracy of the developed COMSOL simulation model. Figures 29–34 show comparison of experimental and simulated transmission, reflection and absorption spectra of the two multi-layer stacks with 15 nm and 30 nm thick Cr layers. Note that the simulation data has been reproduced with data spacing of 2 [cm^{-1}] for better accuracy. In addition, the scales have been adjusted properly so as the comparisons to be as much distinct as possible.

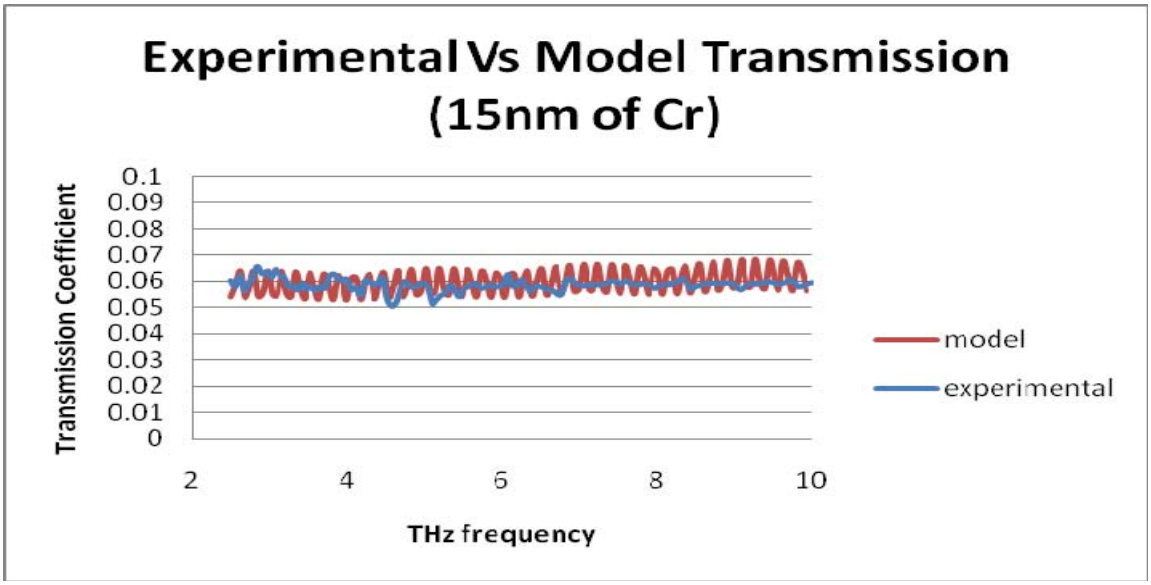

Figure 29. Experimental Versus Simulated Transmission Coefficient of the Multi-layer Stack with 15 nm thick Cr as a Function of THz Frequency

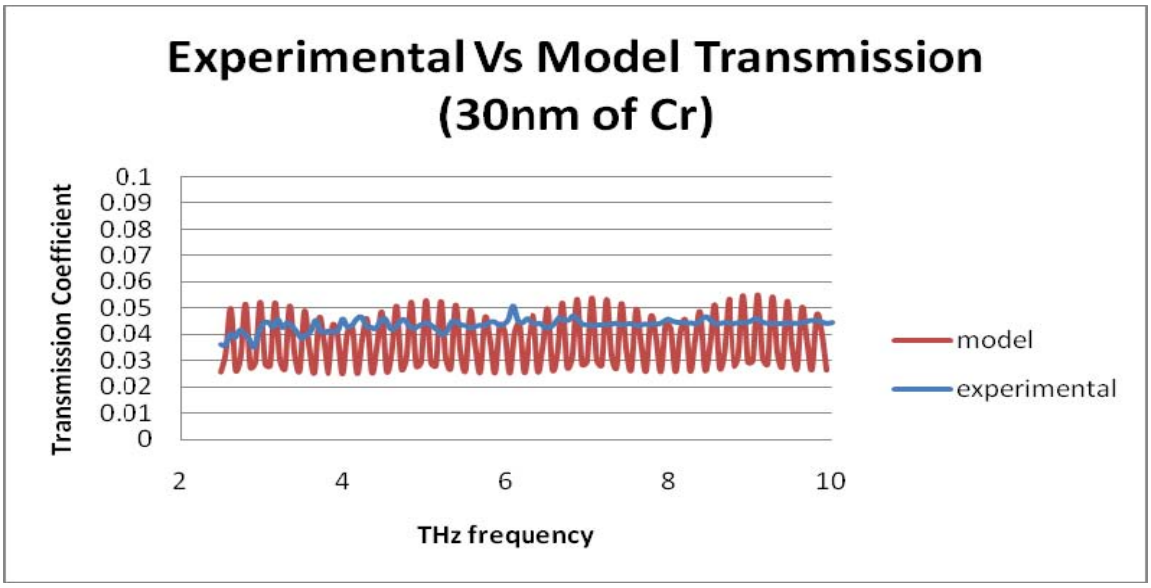

Figure 30. Experimental Versus Simulated Transmission Coefficient of the Multi-layer Stack with 30 nm thick Cr as a Function of THz Frequency

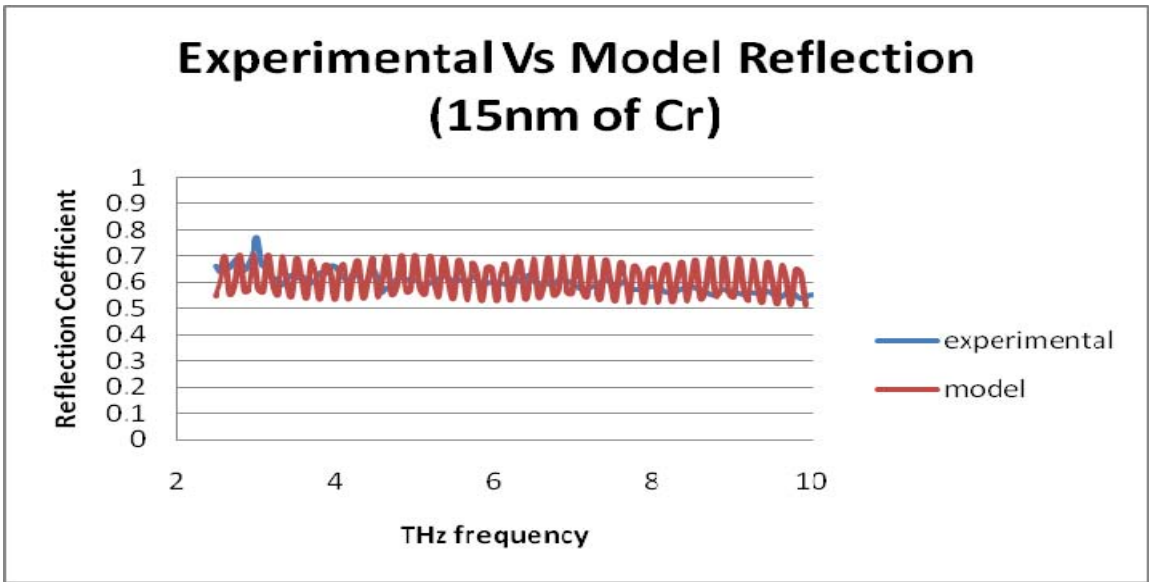

Figure 31. Experimental Versus Simulated Reflection Coefficient of the Multi-layer Stack with 15 nm thick Cr Layer as a Function of THz Frequency

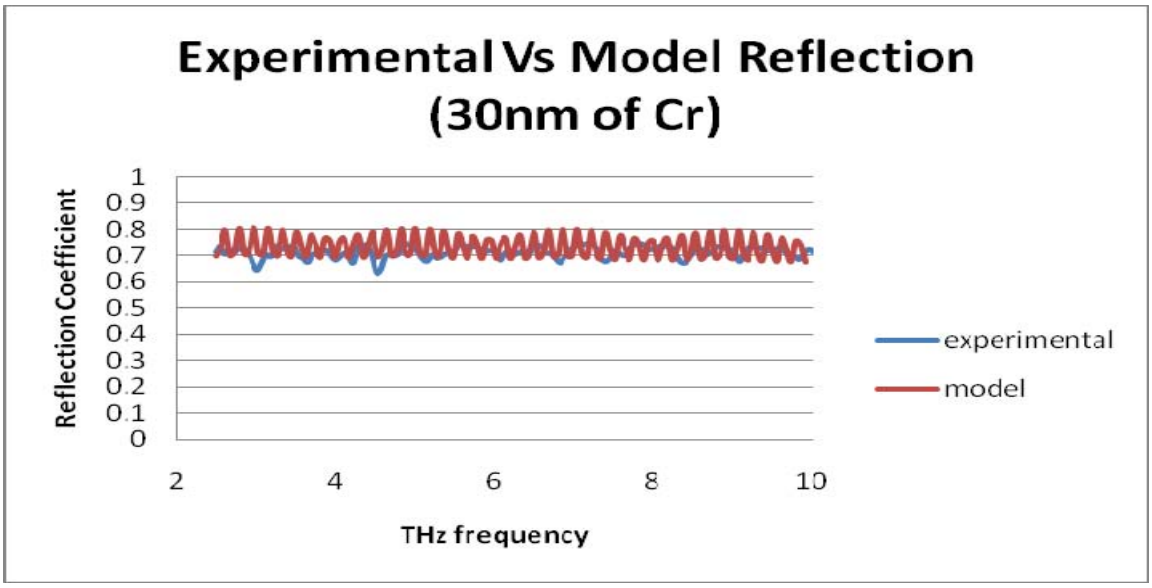

Figure 32. Experimental Versus Simulated Reflection Coefficient of the Multi-layer Stack with 30 nm thick Cr Layer as a Function of THz Frequency

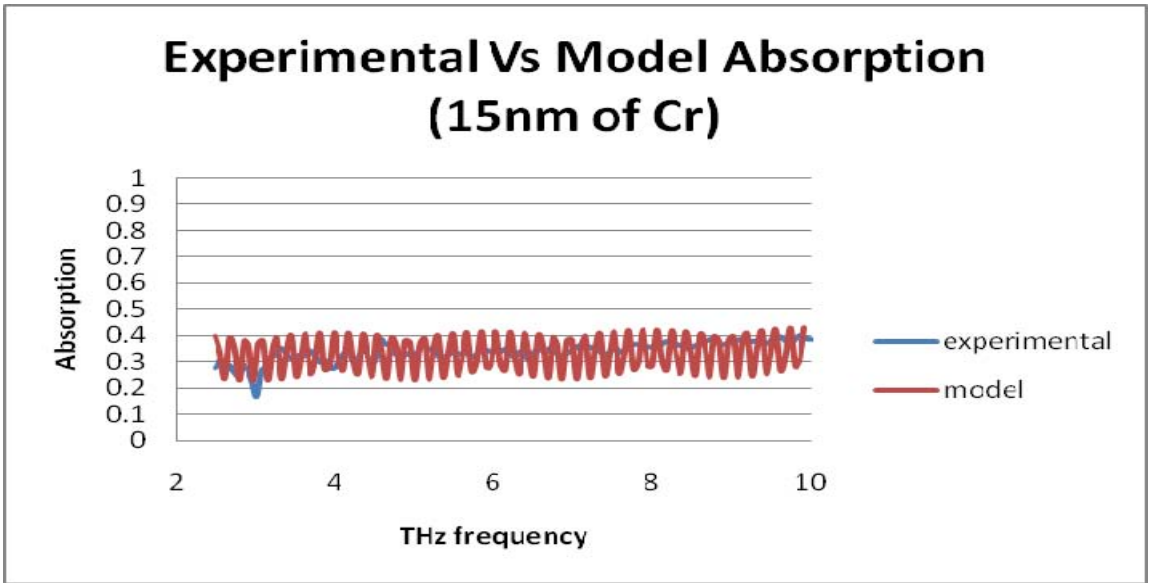

Figure 33. Experimental Versus Simulated Absorption of the Multi-layer Stack with 15 nm Cr Layer as a Function of THz Frequency

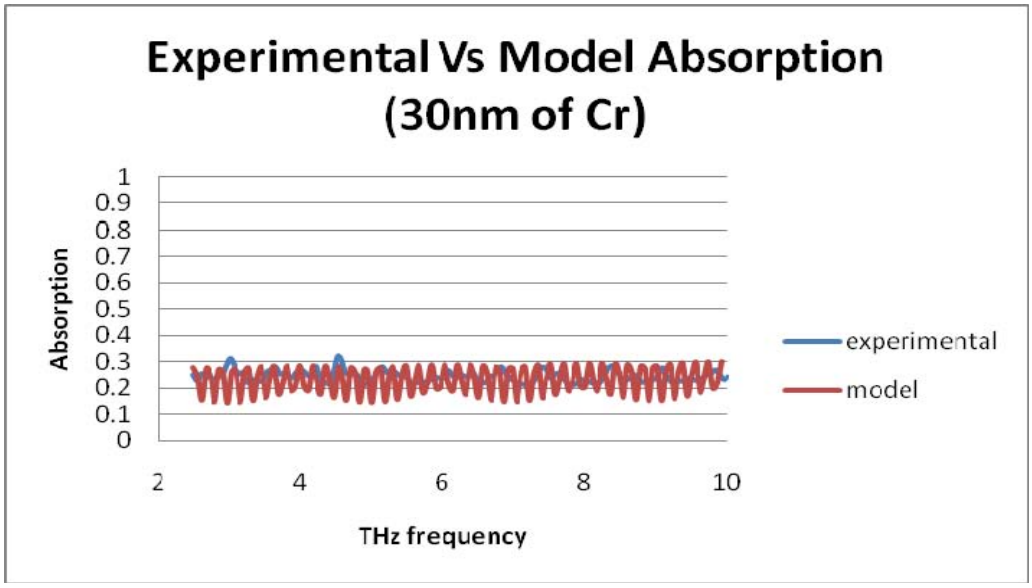

Figure 34. Experimental Versus Simulated Absorption of the Multi-layer Stack with 30 nm Cr Layer as a Function of THz Frequency

It can be seen from the Figures 29–34 that the measurements agrees reasonably well with the finite element simulations done using COMSOL. As mentioned before, the oscillatory behavior seen in simulated data as well as to some extent in the measurements is due to Fabry-Perot effect associated with the Si substrate. In addition, Tables 1 and 2 show comparisons of measured and simulated average values of transmission, reflection and absorption over the 2.5 to 10 THz range for the two multi-layer stacks with 15 nm and 30 nm thick Cr layers. The close agreement between the measurement and simulation shows that modeling can be used for optimizing the thickness of the Cr layer for strong THz absorption.

Table 1. Comparison of Average Coefficients for the Stack with 15 nm thick Cr Layer in the Spectral Region between 2.5 and 10 THz

STACK of 15nm of Cr	Transmission Coefficient (%)	Reflection Coefficient (%)	Absorption (%)
Experimental (Average Value)	**5.87**	**60.06**	**34.07**
Respective standard deviation (%)	0.21	3.6	3.7
Model (Average Value)	**5.98**	**60.02**	**34.00**
Respective standard deviation (%)	0.45	6.1	6.5

Table 2. Comparison of Average Coefficients for the Stack with 15 nm thick Cr Layer in the Spectral Region between 2.5 and 10 THz

STACK of 30nm of Cr	Transmission Coefficient (%)	Reflection Coefficient (%)	Absorption (%)
Experimental (Average Value)	**4.36**	**71.20**	**24.55**
Respective standard deviation (%)	0.22	2.2	2.1
Model (Average Value)	**3.70**	**73.14**	**23.16**
Respective standard deviation (%)	0.99	4.1	5.1

B. ANALYSIS AND OPTIMIZATION

According to Tables 1 and 2, one can notice that a higher reflection resulted when the film thickness is increased from 15 to 30 nm. This is primarily due to the increase in conductivity of the Cr when the thickness is increased. In addition, Tables 1 and 2 also show a significant decrease of average absorption when shifting from 15 nm to 30 nm thickness of Cr layer. Although the transmission decreases, the reflection increases more and as a result the absorption drops. By inspection, one can notice that the increase in reflection is much larger than the transmission decrease. This suggests that the rate of decrease of transmission is smaller than the corresponding rate of increase of reflectance. In other words, as we go to thicker layers of Cr, the average absorption should proportionally decrease.

As it has already mentioned in previous sections, the conductivities of Cr layers were measured to be 6.75 x 105 [S/m] and 7.20 x 105 [S/m] for 15 nm and 30 nm layers, respectively. Assuming a linear dependence of conductivity with the Cr layer thickness simulations can be performed to determine the optimum layer thickness for developing a stack with strong THz absorption. Based on the conductivity data of the two films, each 2 nm increase of Cr layer thickness should represent a 0.046 x 105 [S/m] increase of conductivity.

Since the thin-film stacks employed in THz bi-material pixels will not have the thick Si substrate, it is useful to optimize the absorption of the stack without the substrate. In addition, the angle of incident of THz on the pixel is normal than the 30 degrees used in earlier simulations to compare with experiments. Figures 35–42 show simulated absorption for a set of Cr layer thickness in 1 to 30 nm range as a function of THz frequency. Note that the oscillatory behavior disappeared from the simulated spectra due to removal of the substrate from the model.

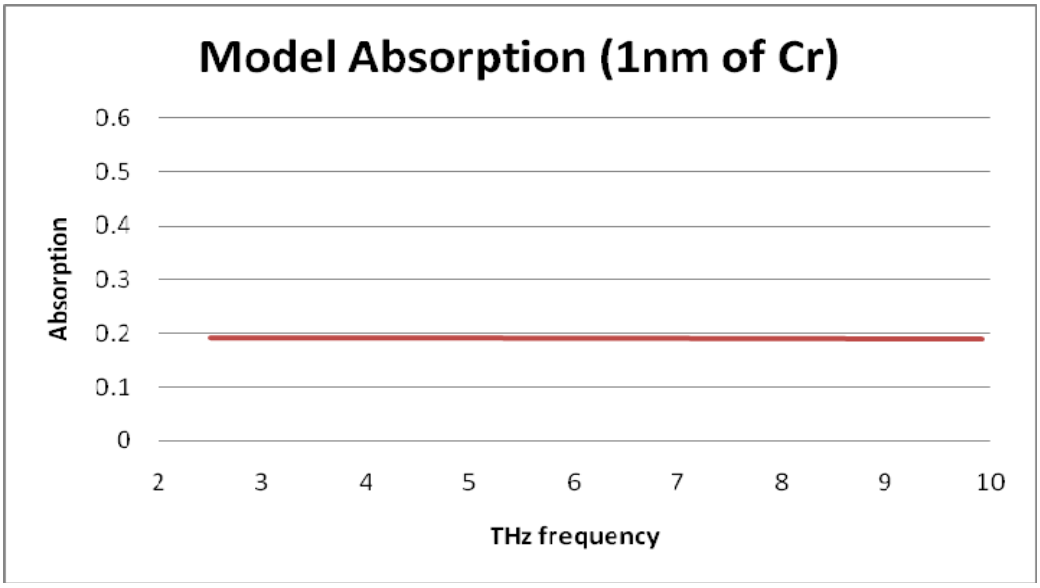

Figure 35. Simulated Absorption of the Multi-layer Stack (without Substrate) with 1 nm thick Cr Layer and Conductivity of 6.428 x 10^5 [S/m] as a Function of THz Frequency

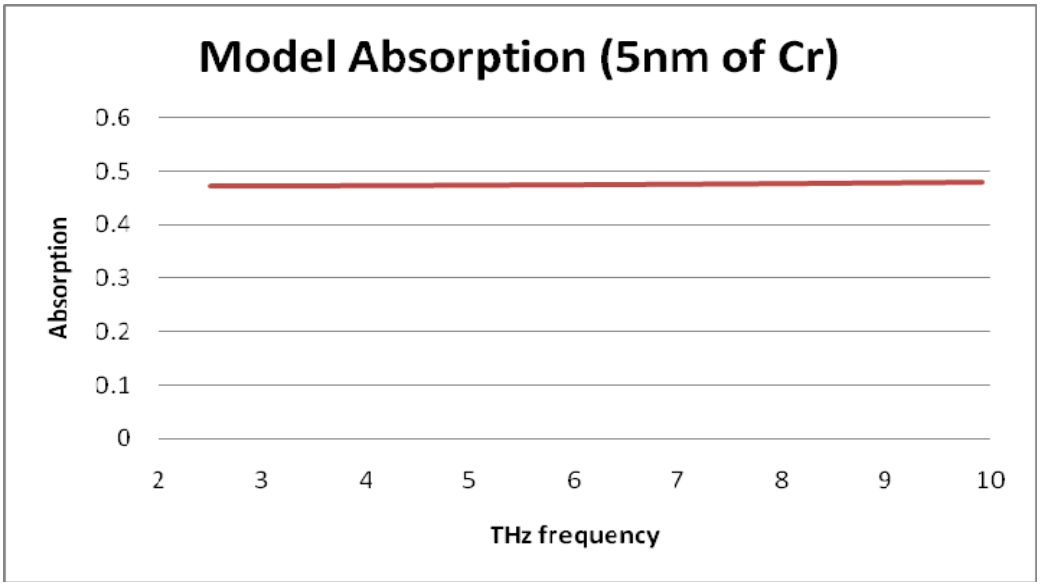

Figure 36. Simulated Absorption of the Multi-layer Stack (without Substrate) with 5 nm thick Cr Layer and Conductivity of 6.520 x 10^5 [S/m] as a Function of THz Frequency

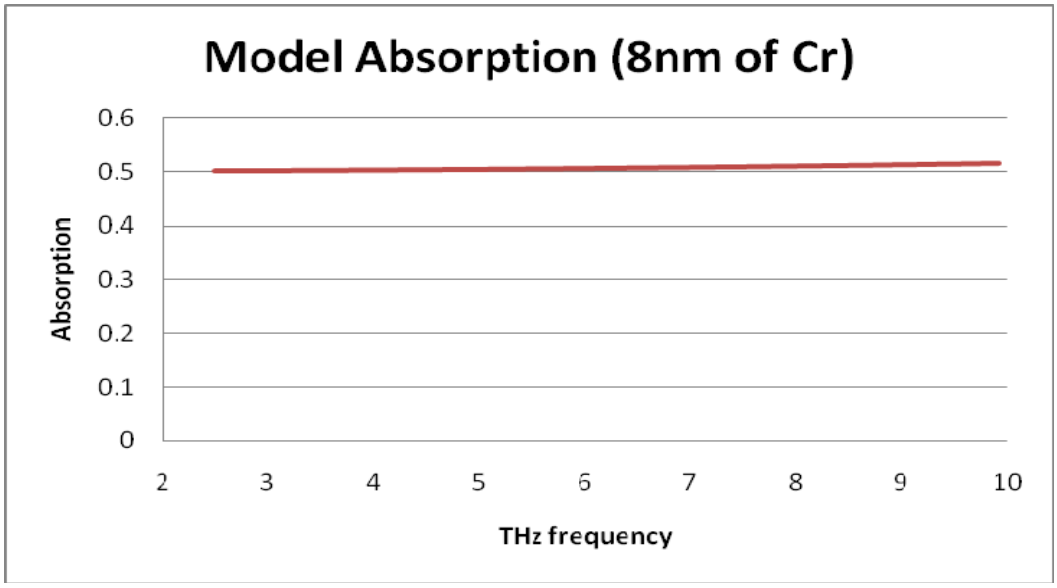

Figure 37. Simulated Absorption of the Multi-layer Stack (without Substrate) with 8 nm thick Cr Layer and Conductivity of 6.589 x 10^5 [S/m] as a Function of THz Frequency

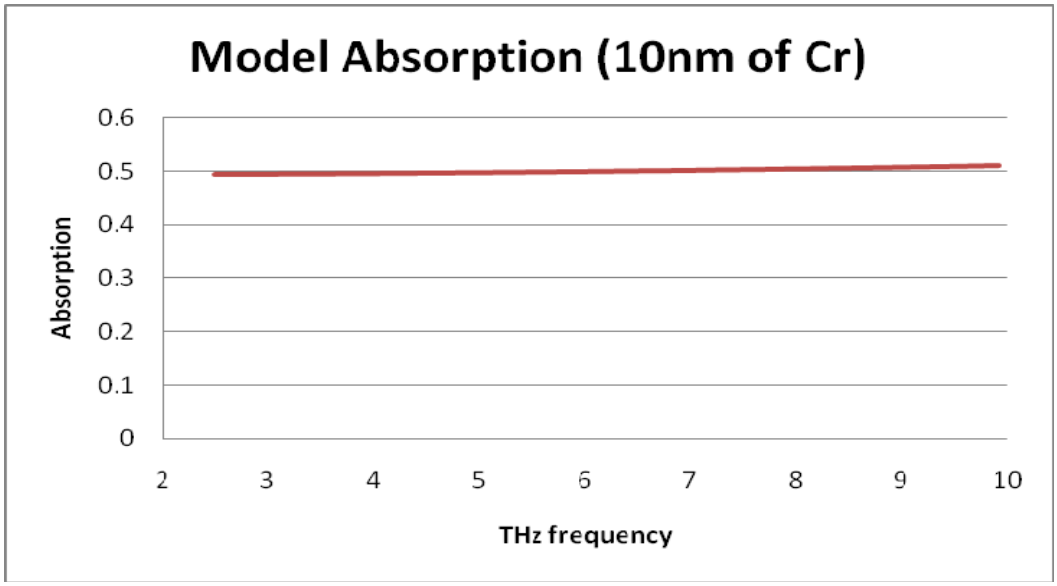

Figure 38. Simulated Absorption of the Multi-layer Stack (without Substrate) with 10 nm thick Cr Layer and Conductivity of 6.635 x 10^5 [S/m] as a Function of THz Frequency

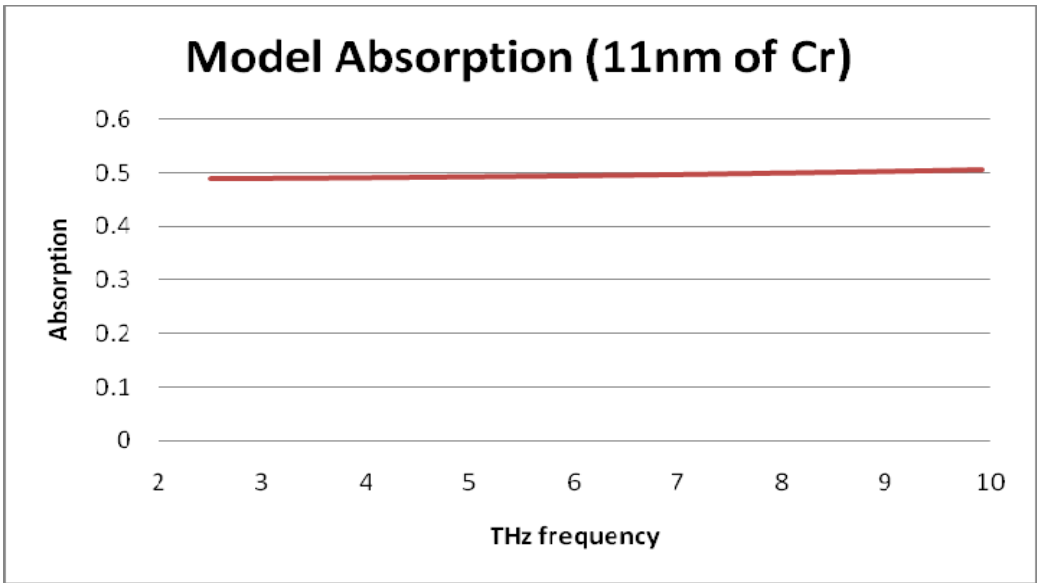

Figure 39. Simulated Absorption of the Multi-layer Stack (without Substrate) with 11 nm thick Cr Layer and Conductivity of 6.658 x 10^5 [S/m] as a Function of THz Frequency

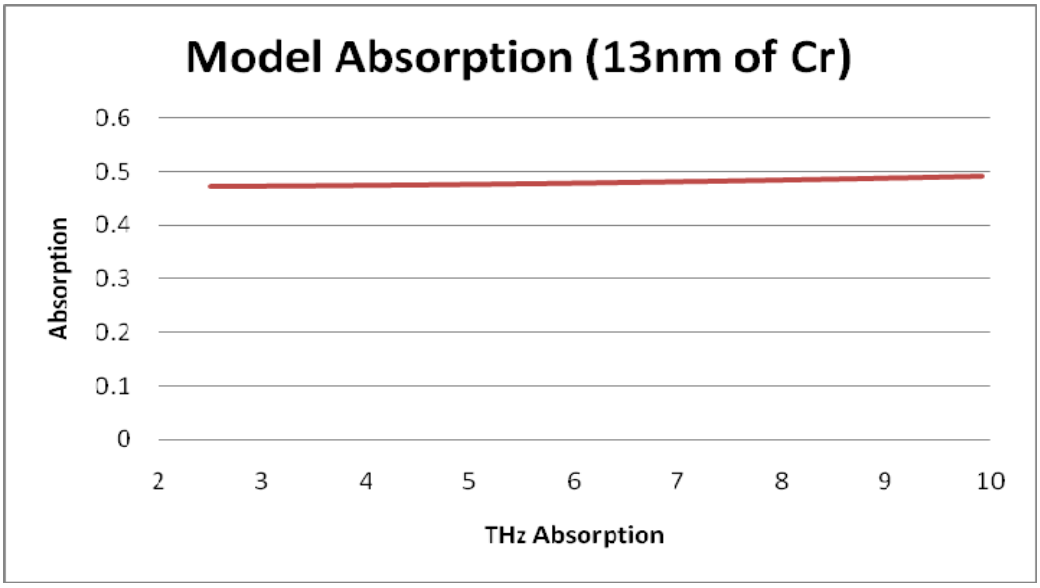

Figure 40. Simulated Absorption of the Multi-layer Stack (without Substrate) with 13 nm thick Cr Layer and Conductivity of 6.704 x 10^5 [S/m] as a Function of THz Frequency

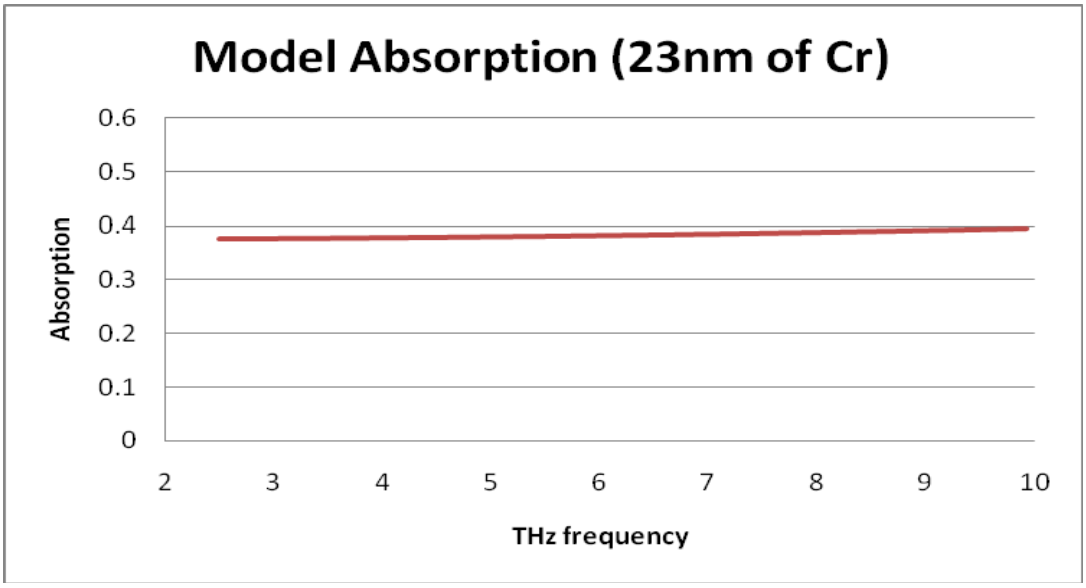

Figure 41. Simulated Absorption of the Multi-layer Stack (without Substrate) with 23 nm thick Cr Layer and Conductivity of 6.934 x 10^5 [S/m] as a Function of THz Frequency

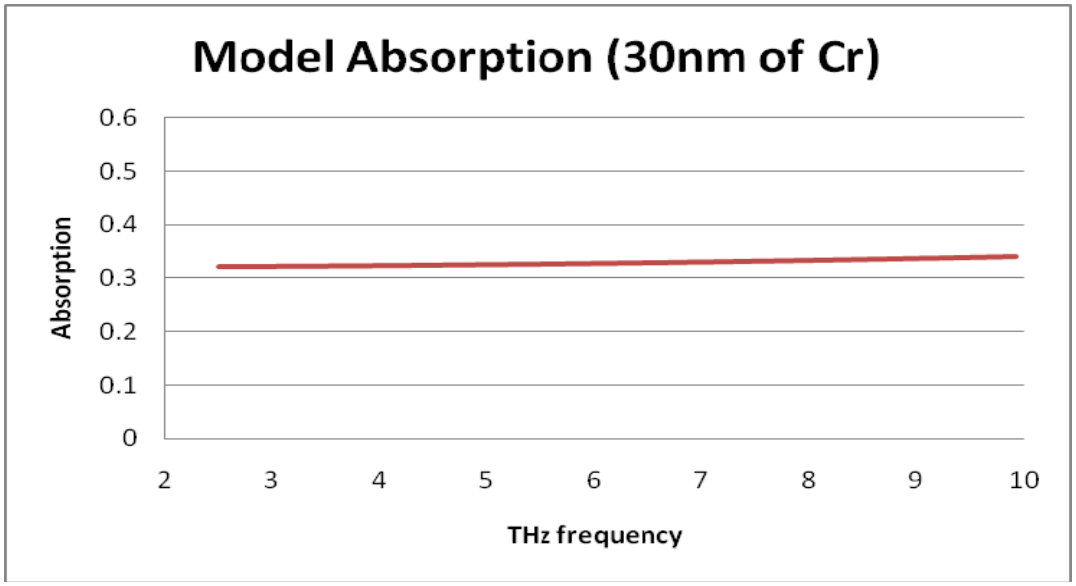

Figure 42. Simulated Absorption of the Multi-layer Stack (without Substrate) with 30 nm thick Cr Layer and Conductivity of 7.095 x 10^5 [S/m] as a Function of THz Frequency

Table 3 shows the averaged values of simulated absorption of the stack over 2.5 to 10 THz range as a function of Cr layer thickness along with the corresponding conductivity values used for simulation. Figure 43 shows a plot of absorption as a function of Cr layer thickness in the 1 to 30 nm range. From the plot in Figure 43, it is obvious that the optimum absorption occurs somewhere between 6 nm to 10 nm thick Cr layer with absorption of about 50% of the incident THz power.

Table 3. Simulated Absorption for the Stack without the Substrate. The Middle Column gives the Conductivities used in the Simulation

***Varying thickness of Cr* [nm]**	Reduced Conductivity of Cr [S/m]	***Modeled Absorption* (%)**
1	6.428×10^5	19.10
5	6.520×10^5	47.46
7	6.566×10^5	50.29
8	6.589×10^5	50.64
9	6.612×10^5	50.55
10	6.635×10^5	50.16
11	6.658×10^5	49.55
13	6.704×10^5	47.94
15	**6.750×10^5**	**46.06**
23	6.934×10^5	38.41
30	7.095×10^5	32.83

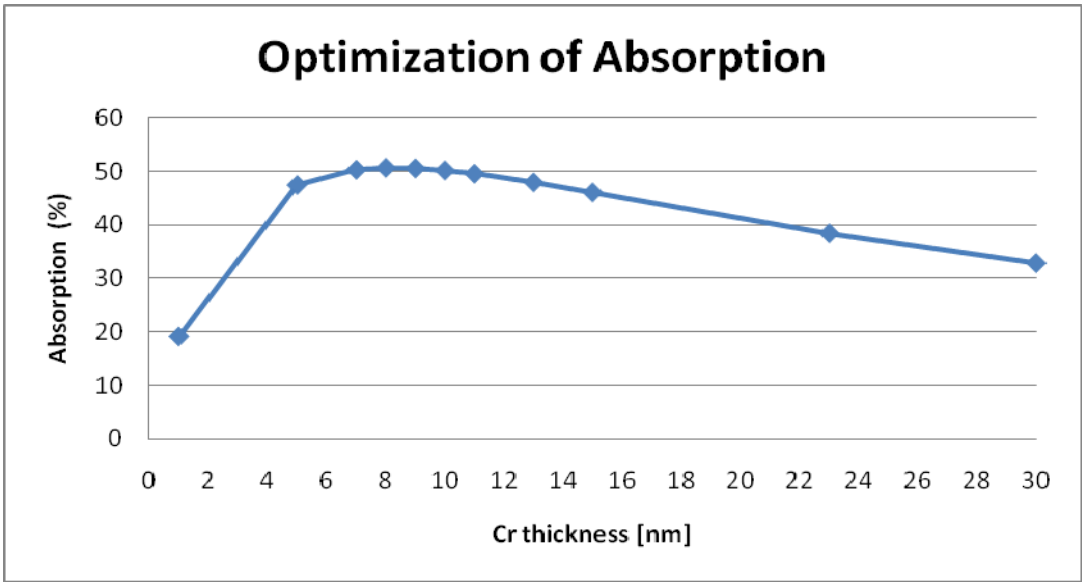

Figure 43. Simualted Absorption of the Multi-layer Stack (without Substrate) as a Function of Chrome Layer Thickness

V. CONCLUSION

In the field of terahertz imaging, the use of MEMS bi-material sensors allows the implementation of optical readout process which can result better signal-to-noise ratio. In addition, it can avoid the integration of readout electronics resulted in a simplified fabrication process. For improving the sensitivity of bi-material pixels for THz imaging, it is necessary to develop high THz absorbing thin films. In this thesis, an accurate model for simulating the absorptive behavior of thin-film materials in the THz range was developed using finite element modeling. The accuracy of the model was compared with calculation done based on the analytical approach described in [9 and 10]. The two approaches gave nearly identical absorption spectra which confirmed the validity of the modeling. In addition, two thin-film stacks containing 15 and 30 nm Cr layers were characterized using FTIR spectroscopy in 2.5 to 10 THz range. It was found that the strength of the absorption decreased from 34 % to 25 % when the film thickness was increased from 15 to 30 nm. This is primarily due to increase in conductivity of the thin film which makes thicker film more reflective. The measured absorption spectra agreed well with that of the simulations indicating the accuracy of the model for describing the absorption in thin films.

The model was used for optimizing the thickness of the Cr layer for achieving strong THz absorption. It was found that a Cr layer of approximately 10 nm gives nearly 50 % absorption of incident THz power. Though the model was developed for Cr metal films, can be generalized to any metal layer of known conductivity. By then taking account the proper functionality of the developed model, the microfabrication of optimized absorptive layers of sub-wavelength thicknesses needed for use in MEMS bi-material detectors, is achievable.

As has previously been stated in this thesis, a significant improvement in THz imaging can be achieved through the respective improvement in the readout technique. Based on a recent research by Thomas Maier [17], microbolometers can be modified by metallic resonant absorber elements leading to an enhanced responsivity at selectable wavelengths. In addition, the dissipative energy absorption of tailored metamaterials

allowed for engineering the response of conventional bolometer microbridges. The absorption peak position and strength could be determined by the geometry of the metamaterial. For square-shaped metal/dielectric metamaterial structure showed spectral resonances at wavelengths between 4.8 μm and 7.0 μm in accordance with numerical simulations using again COMSOL finite element modeling [17] with 80% absorption. The overall results suggest that there could be also a similar application into the THz regime and could also be an interesting objective of a future research.

APPENDIX A: MATLAB CODE DEVELOPED FOR CALCULATING THE TOTAL POWER REFLECTION OF THE MULTI-LAYER STACK

```
n1=1;                                          %Refraction Index of air %
n2=2.05;                  % Refraction Index of Silicon Nitride layer %
n3=1.46;                    % Refraction Index of Silicon Oxide layer %

n4=2.05;  n5=1.46;  n6=2.05;  n7=1.46;  n8=2.05;  n9=1.46;  n10=2.05;
n11=1.46;

n12=(1-i).*4500.*sqrt(lambda);     %Refr. Index of Cr layer, eqn. (4) %
n13=3.42-i.*108.6.*lambda; %Refr. Index of Silicon substrate,eqn. (8) %
n14=1;




d2=0.075e-6;                    % Thickness of Silicon Nitride layer %
d3=0.11e-6;                       % Thickness of Silicon Oxide layer %

d4=0.075e-6; d5=0.11e-6; d6=0.075e-6; d7=0.11e-6;
d8=0.075e-6; d9=0.11e-6; d10=0.075e-6; d11=0.11e-6;

d12=0.015e-6;                             % Thickness of Chrome layer %
d13=500e-6;                          % Thickness of Silicon Substrate %




theta1=pi/6;                                     % Angle of Incidence %

w=8300:200:33300;          % wavenumber range in meters, i.e., 2.5-10THz
%

lambda=1./w;                         % wavelength, as expressed in FTIR %


 % Snell's law for every boundary of the multi-layer stack %

theta2=asin(n1*sin(theta1)/n2);theta3=asin(n1*sin(theta1)/n3);
theta4=asin(n1*sin(theta1)/n4);theta5=asin(n1*sin(theta1)/n5);
theta6=asin(n1*sin(theta1)/n6);theta7=asin(n1*sin(theta1)/n7);
theta8=asin(n1*sin(theta1)/n8);theta9=asin(n1*sin(theta1)/n9);
theta10=asin(n1*sin(theta1)/n10);theta11=asin(n1*sin(theta1)/n11);
theta12=asin(n1.*sin(theta1)./n12);theta13=asin(n1.*sin(theta1)./n13);
theta14=asin(n1.*sin(theta1)./n14);
```

```
 % Change of phase in every layer of the multi-layer stack %

phi2=2*pi./lambda*n2*d2*cos(theta2);phi3=2*pi./lambda*n3*d3*cos(theta3);
phi4=2*pi./lambda*n4*d4*cos(theta4);phi5=2*pi./lambda*n5*d5*cos(theta5);
phi6=2*pi./lambda*n6*d6*cos(theta6);phi7=2*pi./lambda*n7*d7*cos(theta7);
phi8=2*pi./lambda*n8*d8*cos(theta8);phi9=2*pi./lambda*n9*d9*cos(theta9);
phi10=2*pi./lambda*n10*d10*cos(theta10);
phi11=2*pi./lambda*n11*d11*cos(theta11);
phi12=2.*pi./lambda.*n12.*d12.*cos(theta12);
phi13=2.*pi./lambda.*n13.*d13.*cos(theta13);


% Fresnel Coefficients of Reflection for every boundary %

r120=(n1*cos(theta1)-n2*cos(theta2))/(n1*cos(theta1)+n2*cos(theta2));
r23=(n2*cos(theta2)-n3*cos(theta3))/(n2*cos(theta2)+n3*cos(theta3));
r34=(n3*cos(theta3)-n4*cos(theta4))/(n3*cos(theta3)+n4*cos(theta4));
r45=(n4*cos(theta4)-n5*cos(theta5))/(n4*cos(theta4)+n5*cos(theta5));
r56=(n5*cos(theta5)-n6*cos(theta6))/(n5*cos(theta5)+n6*cos(theta6));
r67=(n6*cos(theta6)-n7*cos(theta7))/(n6*cos(theta6)+n7*cos(theta7));
r78=(n7*cos(theta7)-n8*cos(theta8))/(n7*cos(theta7)+n8*cos(theta8));
r89=(n8*cos(theta8)-n9*cos(theta9))/(n8*cos(theta8)+n9*cos(theta9));
r910=(n9*cos(theta9)-n10*cos(theta10))/
(n9*cos(theta9)+n10*cos(theta10));
r1011=(n10*cos(theta10)-n11*cos(theta11))/
(n10*cos(theta10)+n11*cos(theta11));
r1112=(n11.*cos(theta11)-n12.*cos(theta12))./
(n11.*cos(theta11)+n12.*cos(theta12));
r1213=(n12.*cos(theta12)-n13.*cos(theta13))./
(n12.*cos(theta12)+n13.*cos(theta13));
r1314=(n13.*cos(theta13)-n14.*cos(theta14))./
(n13.*cos(theta13)+n14.*cos(theta14));


% Total amplitude reflection for every effective layer %

r13=(r1213+r1314.*exp(-2i.*phi13))./(1+r1213.*r1314.*exp(-2i.*phi13));
r12=(r1112+r13.*exp(-2i.*phi12))./(1+r1112.*r13.*exp(-2i.*phi12));
r11=(r1011+r12.*exp(-2i.*phi11))./(1+r1011.*r12.*exp(-2i.*phi11));
r10=(r910+r11.*exp(-2i*phi10))./(1+r910*r11.*exp(-2i*phi10));
r9=(r89+r10.*exp(-2i*phi9))./(1+r89*r10.*exp(-2i*phi9));
r8=(r78+r9.*exp(-2i*phi8))./(1+r78*r9.*exp(-2i*phi8));
r7=(r67+r8.*exp(-2i*phi7))./(1+r67*r8.*exp(-2i*phi7));
r6=(r56+r7.*exp(-2i*phi6))./(1+r56*r7.*exp(-2i*phi6));
r5=(r45+r6.*exp(-2i*phi5))./(1+r45*r6.*exp(-2i*phi5));
r4=(r34+r5.*exp(-2i*phi4))./(1+r34*r5.*exp(-2i*phi4));
r3=(r23+r4.*exp(-2i*phi3))./(1+r23*r4.*exp(-2i*phi3));
r2=(r120+r3.*exp(-2i*phi2))./(1+r120*r3.*exp(-2i*phi2));


 % TOTAL POWER REFLECTION COEFFICIENT %

R2=r2.*conj(r2);
```

APPENDIX B: MATLAB CODE DEVELOPED FOR CALCULATING THE TOTAL POWER TRANSMISSION OF THE MULTI-LAYER STACK

```
n1=1;                                          %Refraction Index of air %
n2=2.05;                  % Refraction Index of Silicon Nitride layer %
n3=1.46;                    % Refraction Index of Silicon Oxide layer %

n4=2.05;   n5=1.46;   n6=2.05;   n7=1.46;   n8=2.05;   n9=1.46;   n10=2.05;
n11=1.46;

n12=(1-i).*4500.*sqrt(lambda);    %Refr. Index of Cr layer,   eqn.(4) %
n13=3.42-i.*108.6.*lambda; %Refr. Index of Silicon substrate, eqn.(8) %
n14=1;




d2=0.075e-6;                     % Thickness of Silicon Nitride layer %
d3=0.11e-6;                       % Thickness of Silicon Oxide layer %

d4=0.075e-6; d5=0.11e-6; d6=0.075e-6; d7=0.11e-6;
d8=0.075e-6; d9=0.11e-6; d10=0.075e-6; d11=0.11e-6;

d12=0.015e-6;                              % Thickness of Chrome layer %
d13=500e-6;                          % Thickness of Silicon Substrate %




theta1=pi/6;                                      % Angle of Incidence %

w=8300:200:33300;         % wavenumber range in meters, i.e., 2.5-10THz
%

lambda=1./w;                        % wavelength, as expressed in FTIR %



% Snell's law for every boundary of the multi-layer stack %

theta2=asin(n1*sin(theta1)/n2);theta3=asin(n1*sin(theta1)/n3);
theta4=asin(n1*sin(theta1)/n4);theta5=asin(n1*sin(theta1)/n5);
theta6=asin(n1*sin(theta1)/n6);theta7=asin(n1*sin(theta1)/n7);
theta8=asin(n1*sin(theta1)/n8);theta9=asin(n1*sin(theta1)/n9);
theta10=asin(n1*sin(theta1)/n10);theta11=asin(n1*sin(theta1)/n11);
theta12=asin(n1.*sin(theta1)./n12);theta13=asin(n1.*sin(theta1)./n13);
```

```
theta14=asin(n1.*sin(theta1)./n14);



% Change of phase in every layer of the multi-layer stack %

phi2=2*pi./lambda*n2*d2*cos(theta2);phi3=2*pi./lambda*n3*d3*cos(theta3);
phi4=2*pi./lambda*n4*d4*cos(theta4);phi5=2*pi./lambda*n5*d5*cos(theta5);
phi6=2*pi./lambda*n6*d6*cos(theta6);phi7=2*pi./lambda*n7*d7*cos(theta7);
phi8=2*pi./lambda*n8*d8*cos(theta8);phi9=2*pi./lambda*n9*d9*cos(theta9);
phi10=2*pi./lambda*n10*d10*cos(theta10);
phi11=2*pi./lambda*n11*d11*cos(theta11);
phi12=2.*pi./lambda.*n12.*d12.*cos(theta12);
phi13=2*pi./lambda.*n13.*d13.*cos(theta13);


 % Fresnel Coefficients of Reflection for every boundary %

r120=(n1*cos(theta1)-n2*cos(theta2))/(n1*cos(theta1)+n2*cos(theta2));
r23=(n2*cos(theta2)-n3*cos(theta3))/(n2*cos(theta2)+n3*cos(theta3));
r34=(n3*cos(theta3)-n4*cos(theta4))/(n3*cos(theta3)+n4*cos(theta4));
r45=(n4*cos(theta4)-n5*cos(theta5))/(n4*cos(theta4)+n5*cos(theta5));
r56=(n5*cos(theta5)-n6*cos(theta6))/(n5*cos(theta5)+n6*cos(theta6));
r67=(n6*cos(theta6)-n7*cos(theta7))/(n6*cos(theta6)+n7*cos(theta7));
r78=(n7*cos(theta7)-n8*cos(theta8))/(n7*cos(theta7)+n8*cos(theta8));
r89=(n8*cos(theta8)-n9*cos(theta9))/(n8*cos(theta8)+n9*cos(theta9));
r910=(n9*cos(theta9)-n10*cos(theta10))/
(n9*cos(theta9)+n10*cos(theta10));
r1011=(n10*cos(theta10)-n11*cos(theta11))/
(n10*cos(theta10)+n11*cos(theta11));
r1112=(n11.*cos(theta11)-n12.*cos(theta12))./
(n11.*cos(theta11)+n12.*cos(theta12));
r1213=(n12.*cos(theta12)-n13.*cos(theta13))./
(n12.*cos(theta12)+n13.*cos(theta13));
r1314=(n13.*cos(theta13)-n14.*cos(theta14))./
(n13.*cos(theta13)+n14.*cos(theta14));


% Total amplitude reflection for every effective layer %

r13=(r1213+r1314.*exp(-2i.*phi13))./(1+r1213.*r1314.*exp(-2i.*phi13));
r12=(r1112+r13.*exp(-2i.*phi12))./(1+r1112.*r13.*exp(-2i.*phi12));
r11=(r1011+r12.*exp(-2i.*phi11))./(1+r1011.*r12.*exp(-2i.*phi11));
r10=(r910+r11.*exp(-2i*phi10))./(1+r910*r11.*exp(-2i*phi10));
r9=(r89+r10.*exp(-2i*phi9))./(1+r89*r10.*exp(-2i*phi9));
r8=(r78+r9.*exp(-2i*phi8))./(1+r78*r9.*exp(-2i*phi8));
r7=(r67+r8.*exp(-2i*phi7))./(1+r67*r8.*exp(-2i*phi7));
r6=(r56+r7.*exp(-2i*phi6))./(1+r56*r7.*exp(-2i*phi6));
r5=(r45+r6.*exp(-2i*phi5))./(1+r45*r6.*exp(-2i*phi5));
r4=(r34+r5.*exp(-2i*phi4))./(1+r34*r5.*exp(-2i*phi4));
r3=(r23+r4.*exp(-2i*phi3))./(1+r23*r4.*exp(-2i*phi3));
r2=(r120+r3.*exp(-2i*phi2))./(1+r120*r3.*exp(-2i*phi2));
```

```
 % Fresnel Coefficients of Transmission for every boundary %

t120=(2*n1*cos(theta1))/(n1*cos(theta1)+n2*cos(theta2));
t23=(2*n2*cos(theta2))/(n2*cos(theta2)+n3*cos(theta3));
t34=(2*n3*cos(theta3))/(n3*cos(theta3)+n4*cos(theta4));
t45=(2*n4*cos(theta4))/(n4*cos(theta4)+n5*cos(theta5));
t56=(2*n5*cos(theta5))/(n5*cos(theta5)+n6*cos(theta6));
t67=(2*n6*cos(theta6))/(n6*cos(theta6)+n7*cos(theta7));
t78=(2*n7*cos(theta7))/(n7*cos(theta7)+n8*cos(theta8));
t89=(2*n8*cos(theta8))/(n8*cos(theta8)+n9*cos(theta9));
t910=(2*n9*cos(theta9))/(n9*cos(theta9)+n10*cos(theta10));
t1011=(2*n10*cos(theta10))/(n10*cos(theta10)+n11*cos(theta11));
t1112=(2.*n11.*cos(theta11))./(n11.*cos(theta11)+n12.*cos(theta12));
t1213=(2.*n12.*cos(theta12))./(n12.*cos(theta12)+n13.*cos(theta13));
t1314=(2.*n13.*cos(theta13))./(n13.*cos(theta13)+n14.*cos(theta14));



% Total amplitude transmission for every effective layer %

t13=(t1213.*t1314.*exp(-i.*phi13))./(1+r1213.*r1314.*exp(-2i.*phi13));
t12=(t1112.*t13.*exp(-i.*phi12))./(1+r1112.*r13.*exp(-2i.*phi12));
t11=(t1011*t12.*exp(-i.*phi11))./(1+r1011*r12.*exp(-2i*phi11));
t10=(t910.*t11.*exp(-i.*phi10))./(1+r910.*r11.*exp(-2i.*phi10));
t9=(t89.*t10.*exp(-i.*phi9))./(1+r89.*r10.*exp(-2i.*phi9));
t8=(t78.*t9.*exp(-i.*phi8))./(1+r78.*r9.*exp(-2i.*phi8));
t7=(t67.*t8.*exp(-i.*phi7))./(1+r67.*r8.*exp(-2i.*phi7));
t6=(t56.*t7.*exp(-i.*phi6))./(1+r56*r7.*exp(-2i.*phi6));
t5=(t45.*t6.*exp(-i.*phi5))./(1+r45.*r6.*exp(-2i.*phi5));
t4=(t34.*t5.*exp(-i.*phi4))./(1+r34*r5.*exp(-2i.*phi4));
t3=(t23.*t4.*exp(-i.*phi3))./(1+r23.*r4.*exp(-2i.*phi3));
t2=(t120.*t3.*exp(-i.*phi2))./(1+r120*r3.*exp(-2i.*phi2));



% TOTAL POWER TRANSMISSION COEFFICIENT %

T2=(n14.*cos(theta14)./(n1.*cos(theta1))).*t2.*conj(t2);
```

THIS PAGE INTENTIONALLY LEFT BLANK

LIST OF REFERENCES

[1] P. Y. Han, G. C. Cho, and X.-C. Zhang, "Time-domain transillumination of biological tissues with terahertz pulses," Optics Letters **25**, p. 242–244 (2000).

[2] P. Bakopoulos, et al, "A tunable Continuous Wave (CW) and Short-pulse Optical Source for THz Brain Imaging Applications," Meas. Sci. Technol. **20** (2009).

[3] A. W. M. Lee, B. S. Williams, S. Kumar, Q. Hu, J. L. Reno, "Real-Time Imaging Using a 4.3-THz Quantum Cascade Laser and a 320 240 Microbolometer Focal-Plane Array," IEEE Photonics Technology Letters, **18** (13), p. 1415 (2006).

[4] R. S. Quimby, "Photonics and Lasers. An Introduction," Wiley-Interscience, 2006.

[5] J. F. de Boer, et al, "Improved Signal-to-Noise Ratio in Spectral Domain compared with Time-domain Optical Coherence tomography," Optics Letters **28** (21), p. 2067-2069 (2003).

[6] D. Grbovic, "Imaging by Detection of Infrared Photons Using Arrays of Uncooled Micromechanical Detectors," PhD diss., University of Tennessee, 2008.

[7] D. Grbovic and G. Karunasiri, "Fabrication of Bi-material MEMS detector arrays for THz imaging," Proc. SPIE 7311, 731108 (2009).

[8] C. C. Homes, "Fourier Transform Infrared Spectroscopy," Brookhaven National Laboratory, January 2007.

[9] P. Lecaruyer, E. Maillart, M. Canva, and J. Rolland, "Generalization of the Rouard Method to an Absorbing Thin-film Stack and Application to Surface Plasmon Resonance," Applied Optics **45**(33), p. 8419–8423, (2006).

[10] Born and Wolf, "Principles of Optics 7^{th} edition (expanded)," Cambridge University, 1999.

[11] N. Laman, and D. Grischkowsky, "Terahertz Conductivity of Thin Metal Films," Applied Physics, **93**(5), p. 051105 (2008).

[12] Jacques I. Pankove, "Optical Processes in Semiconductors," Dover, 1971.

[13] COMSOL AB, "Introductory Tutorial to the RF Module: Periodic Problems & Diffraction Gratings," Copyright 2009.

[14] R. G. Lyons, "Understanding Digital Signal Processing," Kindle, July 2007.

[15] Thermo Nicolet Corporation, “870 User’s Guide,” Madison, 1999.

[16] C. Bolakis, D. Grbovic, G. Karunasiri, and N. V. Lavrik, “Fabrication of high Terahertz-Absorbing stack of dielectric and metal thin films,” submitted to Optics Express.

[17] T. Maier and H. Bruckl, “Wavelength-Tunable Microbolometers with Metamaterial Absorbers,” Optics Letters **34** (19), p.3012 (2009).

INITIAL DISTRIBUTION LIST

1. Defense Technical Information Center
   Ft. Belvoir, Virginia

2. Dudley Knox Library
   Naval Postgraduate School
   Monterey, California

3. Graduate School of Engineering and Applied Sciences
   Naval Postgraduate School
   Monterey, California

4. Associate Professor Gamani Karunasiri
   Department of Physics
   Naval Postgraduate School
   Monterey, California

5. Research Associate Dragoslav Grbovic
   Department of Physics
   Naval Postgraduate School
   Monterey, California

6. Professor and Chairman Andres Larraza
   Department of Physics
   Naval Postgraduate School
   Monterey, California

7. Christos Bolakis
   Naval Postgraduate School
   Monterey, California